A Novel Ultra-Massive MIMO BDCM for 6G Wireless Communication Systems

Yi Zheng, Cheng-Xiang Wang, *Fellow, IEEE*, Jie Huang, *Member, IEEE*, Rui Feng, *Member, IEEE*, and John Thompson, *Fellow, IEEE*

Abstract

In this paper, a novel beam domain channel model (BDCM) for sixth generation (6G) ultra-massive multiple-input multiple-output (MIMO) wireless communication systems is proposed by transforming from an existing geometry-based stochastic model (GBSM). Both the GBSM and BDCM consider the special channel characteristics of ultra-massive MIMO, including spherical wavefront and spatial non-stationarity properties. Steering vectors of the spherical wavefront are derived by higher-order Taylor expansion. By sampling the angle and distance rings, steering matrices of the spherical wavefront can be transformed to unitary matrices. This helps to achieve a perfect transformation from the GBSM to the BDCM in the near-field condition. Meanwhile, it opens up a view of beam domain for channel characteristic analysis to reduce the model complexity. Common statistical properties of the GBSM and BDCM in the near-field and simplified far-field conditions are studied, including spatial cross-correlation functions (SCCFs), temporal autocorrelation functions (TACFs), frequency correlation functions (FCFs), etc. Specific statistical properties, such as the root mean square (RMS) angular spread of

Y. Zheng, C.-X. Wang, and J. Huang are with the National Mobile Communications Research Laboratory, School of Information Science and Engineering, Southeast University, Nanjing 210096, China, and also with the Purple Mountain Laboratories, Nanjing 211111, China (email: {zheng_yi, chxwang, j_huang}@seu.edu.cn).

R. Feng is with Purple Mountain Laboratories, Nanjing 211111, China, and also with the National Mobile Communications Research Laboratory, School of Information Science and Engineering, Southeast University, Nanjing 210096, China (e-mail: fengrui@pmlabs.com.cn).

J. Thompson is with the Institute for Digital Communications, School of Engineering, University of Edinburgh, Edinburgh EH9 3JL, U.K. (e-mail: john.thompson@ed.ac.uk).

the GBSM and RMS beam spread of the BDCM, are studied. Channel capacities of the GBSM and BDCM are investigated and compared with measurement data. It turns out that simulated capacities considering near-field conditions show good agreements with measured capacities. On the other hand, simulated capacities considering far field conditions show a large discrepancy with measured capacities. This indicates that near-field effects need to be included in the channel modeling and performance evaluation of 6G ultra-massive MIMO communication systems.

Index Terms

Ultra-massive MIMO, near-field, channel characteristics, GBSM, BDCM.

I. INTRODUCTION

The vision of the sixth generation (6G) communication network was proposed in [1], [2], including global coverage, all spectra, full applications, and strong security. As one of the full application scenarios, ultra-massive multiple-input multiple-output (MIMO) technology attracts more and more attention [3]–[8]. Accurate ultra-massive MIMO channel characteristics and channel models are needed for future communication system design and performance evaluation, which requires further study.

Typical channel characteristics of massive MIMO are verified by channel measurements, including spherical wavefront, spatial non-stationarity, channel hardening, and sparsity in the beam domain. In [9], [10], channel measurements were conducted at 2.6 GHz with a 50 MHz bandwidth. The base station (BS) was equipped with a 128-element virtual uniform linear array (ULA) acting as the receiver (Rx) and a single antenna user equipment (UE) was used as the transmitter (Tx). Variations of the Rician factor and channel gain along the array verified the spatial non-stationarity. In addition, the line-of-sight (LoS) path of the angular power spectral density (PSD) drifting over the array verified the spherical wavefront property. Channel measurements were conducted at 1.4725 GHz with a bandwidth of 91 MHz in outdoor stadium scenarios in [11], [12]. The BS was equipped with a 128-element virtual ULA. The angle of departure (AoD) drifting along the ULA verified the spherical wavefront property. In [13], [14], ultra-massive MIMO channel measurements were conducted at 5.3 GHz with a bandwidth of 160 MHz in an urban scenario. The Rx was equipped with a 128×8 ultra-massive MIMO antenna array. The Tx was arranged in two configurations, one was a single-user configuration and the other was a multi-user configuration. For the single-user configuration, the Tx was equipped with

8 antennas. For the multi-user configuration, the Tx comprised 4 UEs. Each UE was equipped with 4 antennas. All the above mentioned channel characteristics need to be modeled accurately for 6G performance evaluation.

In the literature, stochastic channel models for massive MIMO communications can be classified as geometry-based stochastic models (GBSMs), correlation-based stochastic models (CBSMs) [15], [16], and beam domain channel models (BDCMs) [17]. In [18], a twin-cluster GBSM was proposed, which considered spherical wavefront and spatial non-stationarity. In [19], a three-dimensional (3D) cluster-based double-spherical GBSM for terahertz (THz) ultra-massive MIMO systems was proposed. In [20], a 3D space-time-frequency (STF) non-stationary GBSM for THz ultra-massive MIMO systems was proposed. In [21], a GBSM using the second-order approximation for modeling the spherical wavefront was proposed. In addition, cluster birth-death process and smooth variations of the clusters' average power along the array and time axes were modeled. In [22], a novel unified GBSM framework for fifth generation (5G) wireless communication systems was proposed. A novel 3D non-stationary GBSM for 5G and beyond 5G (B5G) systems was presented in [23]. It combined different channel properties into a general model framework. In addition, the proposed GBSM was able to be applied to multiple frequency bands and multiple scenarios, which included the ultra-massive MIMO communication scenario. All the above mentioned GBSMs were focused on studying channel characteristics of the array domain. Note that the GBSM superimposes all the multipath components (MPCs) in the array domain. The complexity of the GBSM increases with the number of antennas. The BDCM can separate MPCs of different angles by different beams. The channel matrix of the BDCM is more sparse than that of the GBSM. This means that most channel coefficients of the normalized channel matrix tend to zero. This helps to reduce the complexity in signal processing and assist in algorithm design [24]–[27]. In [28], the complexities of a GBSM and the corresponding BDCM were studied and compared. It was shown that the complexity of the BDCM was lower than that of the GBSM. Therefore, it is of great significance to study BDCMs and the corresponding channel characteristics.

In [27], a BDCM was proposed on the far-field assumption, which meant that the scatterers were far away from the BS and the angular spread at the BS side was relatively small. When the number of antennas at the BS side tended to infinity, the gains of the BDCM became independent of the sub-carrier index. This revealed the frequency-flat property of channel gains in the beam domain. In [29], the proposed BDCM, based on the far-field assumption, was used to assist

the analysis of the power allocation algorithm. In [30], a framework for accurate computational modeling of a continuous aperture phased (CAP) MIMO system was proposed. It was based on a finite-dimensional system representation induced by critical sampling of antenna apertures. Thus, it provided a framework for virtual modeling of continuous aperture systems. In [31], the massive MIMO channel model of the beam domain in THz systems was used to assist channel tracking. In [32], the channel model of beam domain was obtained from the Saleh-Valenzuela channel model. It was used to assist in maximizing the minimal rate of MIMO using non-orthogonal multiple access (NOMA) in the single-beam and multi-beam cases. In [33], [34], channel models of the beam domain for millimeter wave (mmWave) massive MIMO systems were proposed for channel estimation. However, the above mentioned BDCMs were based on far-field assumptions and spatial non-stationarity effects were not well modeled. In [35], a 28 GHz CAP MIMO prototype was introduced and the channel measurement result of the delay PSD was studied. In [36], a novel BDCM was proposed incorporating the effect of array non-stationarity. However, the model was also based on far-field assumption.

A two-dimensional (2D) BDCM based on wideband elliptic model was proposed in [28]. The model considered both spherical wavefront and spatial non-stationarity effects. However, it did not consider the difference of channel characteristics between the near-field and far-field steering vectors. In [37], a BDCM considering both spherical wavefront and spatial non-stationarity effects was obtained from the transformation of the GBSM through designed block transformation matrix. However, the propagation distance difference between different sub-arrays was difficult to obtain. To the best of the authors' knowledge, there is no BDCM considering both spherical wavefront and spatial non-stationarity effects and being obtained from the transformation of GBSM by available unitary matrices under near-field and simplified far-field conditions. In addition, studying and comparing the difference of the channel characteristics using steering matrices under near-field and simplified far-field conditions with measurement data are still insufficient. To fill this gap, a novel BDCM is proposed. The main contributions and novelties of this paper are summarized as follows.

1) A novel ultra-massive MIMO BDCM is proposed, which is transformed from the GBSM. Both of them consider special ultra-massive MIMO channel characteristics, including spherical wavefront and spatial non-stationarity. Steering vectors of the spherical wavefront are derived by the method of higher-order Taylor expansion and can be simplified to those of plane wavefront. The spatial non-stationarity effects are modeled by the cluster birth-

death process along the antenna array.

2) By sampling the angle and distance rings, steering matrices of the spherical wavefront can be transformed to unitary matrices. In addition, steering matrices of the plane wavefront are unitary matrices. This achieves a perfect transformation from the GBSM to the BDCM in both near-field and far-field conditions.

3) Statistical properties of the GBSM and BDCM for steering matrices of the spherical wavefront and plane wavefront are studied and compared, including spatial cross-correlation functions (SCCFs), temporal autocorrelation functions (TACFs), frequency correlation functions (FCFs), root mean square (RMS) angular spread, RMS beam spread, etc. In addition, channel capacities are investigated. Good agreement between simulation results and measurement results verifies the accuracy of the GBSM and BDCM using steering matrices of the spherical wavefront for near-field communications.

The rest of this paper is organized as follows. Section II presents the ultra-massive MIMO GBSM in details. In Section III, the BDCM transformed from the GBSM is shown. In Section IV, we derive statistical properties and channel capacities of the ultra-massive MIMO GBSM and BDCM. In Section V, we present results and analysis. Finally, conclusions are drawn in Section VI.

II. THE ULTRA-MASSIVE MIMO GBSM

Let us assume that the BS side is the Tx and the UE side is the Rx. There are M_T transmit antennas for the BS and M_R receive antennas for the UE. The received signal is the superposition of MPCs, including the LoS path and non-line-of-sight (NLoS) components. As illustrated in Fig. 1, the GBSM is based on the twin-cluster model in [13]. ULAs are employed at both the Tx and Rx sides. The pth transmit and qth receive antennas are denoted as $A_p^T(p = 1, 2, \cdots, M_T)$ and $A_q^R(q = 1, 2, \cdots, M_R)$, respectively. The distances between adjacent antenna elements are δ_T at the Tx side and δ_R at the Rx side. The azimuth and elevation angles of the Tx antenna array are written as β_A^T and β_E^T, respectively. The azimuth and elevation angles of the Rx antenna array are written as β_A^R and β_E^R, respectively. The twin-cluster model can be simplified to a single-cluster model when the first bounce cluster C_n^A at the Tx side and the last bounce cluster C_n^Z at the Rx side completely overlap [18], [38]. Note that there are $N(t)$ clusters in total and one cluster contains $M_n(t)$ scatterers. The standard derivations of scatterers' azimuth angle of departure (AAoD) distribution, azimuth angle of arrival (AAoA) distribution, elevation angle of

departure (EAoD) distribution, elevation angle of arrival (EAoA) distribution, and delays from the Tx or Rx to scatterers in one cluster are expressed as σ_{ASD}, σ_{ASA}, σ_{ESD}, σ_{ESA}, and σ_{DS}, respectively [13]. For clarity, some key parameters of the GBSM are shown in Table I, other key parameters are the same as those in Table III in [13].

A. Channel Matrix

The channel matrix of the GBSM can be expressed as

$$\mathbf{H}(t,f) = \sqrt{\frac{K_{RF}(t)}{K_{RF}(t)+1}}\mathbf{H}^L(t,f) + \sqrt{\frac{1}{K_{RF}(t)+1}}\mathbf{H}^N(t,f) \tag{1}$$

where $\mathbf{H}^L(t,f)$ and $\mathbf{H}^N(t,f)$ are the LoS path and NLoS components for the channel matrix of the GBSM, respectively. The Rician factor is expressed as $K_{RF}(t)$. Note that $\mathbf{H}(t,f)$, $\mathbf{H}^L(t,f)$, and $\mathbf{H}^N(t,f)$ are $M_R \times M_T$ matrices. Considering radiation patterns of antenna elements with vertical polarization and horizontal polarization, $\mathbf{H}^L(t,f)$ and $\mathbf{H}^N(t,f)$ can be further expressed as [36], [39], [40]

$$\mathbf{H}^L(t,f) = \mathbf{a}_{R,L} \begin{bmatrix} F_{V_p}\big(\phi^R_{E,L}(t),\phi^R_{A,L}(t)\big) \\ F_{H_p}\big(\phi^R_{E,L}(t),\phi^R_{A,L}(t)\big) \end{bmatrix}^T \begin{bmatrix} e^{\mathrm{j}\theta^{V_p V_p}_L} & 0 \\ 0 & -e^{\mathrm{j}\theta^{H_p H_p}_L} \end{bmatrix} \begin{bmatrix} F_{V_p}\big(\phi^T_{E,L}(t),\phi^T_{A,L}(t)\big) \\ F_{H_p}\big(\phi^T_{E,L}(t),\phi^T_{A,L}(t)\big) \end{bmatrix}$$
$$\times\, e^{\mathrm{j}2\pi(f_c-f)\tau^L_{11}(t)}\mathbf{a}^H_{T,L} \tag{2}$$
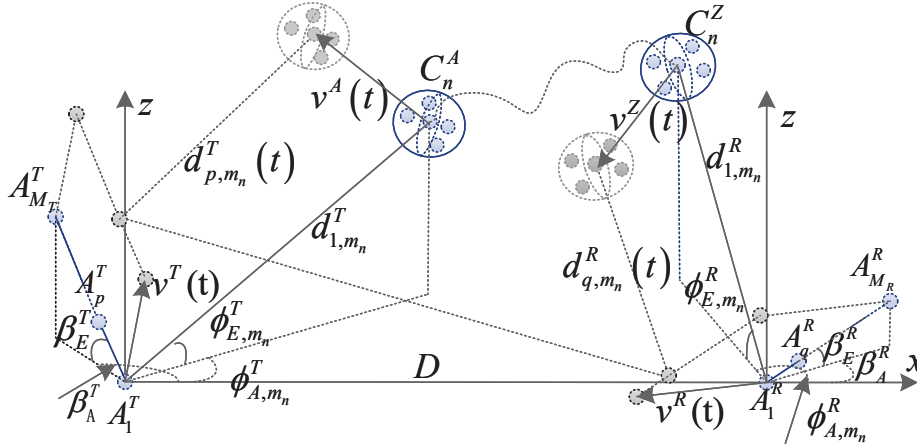
Fig. 1. A 3D ultra-massive MIMO GBSM.

TABLE I. DEFINITIONS OF SOME KEY CHANNEL MODEL PARAMETERS.

Parameters	Definitions
$\vec{d}_{1,m_n}^T(t)$	Distance vector between the first antenna A_1^T and the mth scatterer in the nth cluster at time t
$\vec{d}_{1,m_n}^R(t)$	Distance vector between the first antenna A_1^R and the mth scatterer in the nth cluster at time t
$\tau_{11,m_n}(t)$	Delay from the antenna A_1^T through the mth scatterer in the nth cluster to the antenna A_1^R at time t
$P_{11,m_n}(t)$	Power of the ray from the antenna A_1^T through the mth scatterer in the nth cluster to the antenna A_1^R at time t
$P_{qp,m_n}(t)$	Power of the ray from the antenna A_p^T through the mth scatterer in the nth cluster to the antenna A_q^R at time t

and

$$\mathbf{H}^N(t,f) = \sqrt{\mathbf{P}_{m_n}(t)} \odot \sum_{n=1}^{N(t)} \sum_{m=1}^{M_n(t)} \mathbf{a}_{R,m_n} \begin{bmatrix} F_{V_p}\left(\phi_{E,m_n}^R(t), \phi_{A,m_n}^R(t)\right) \\ F_{H_p}\left(\phi_{E,m_n}^R(t), \phi_{A,m_n}^R(t)\right) \end{bmatrix}^T$$

$$\times \begin{bmatrix} e^{\mathrm{j}\theta_{mn}^{V_p V_p}} & \sqrt{\kappa_{m_n}^{-1}(t)} e^{\mathrm{j}\theta_{mn}^{V_p H_p}} \\ \sqrt{\kappa_{m_n}^{-1}(t)} e^{\mathrm{j}\theta_{mn}^{H_p V_p}} & e^{\mathrm{j}\theta_{mn}^{H_p H_p}} \end{bmatrix} \begin{bmatrix} F_{V_p}\left(\phi_{E,m_n}^T(t), \phi_{A,m_n}^T(t)\right) \\ F_{H_p}\left(\phi_{E,m_n}^T(t), \phi_{A,m_n}^T(t)\right) \end{bmatrix}$$

$$\times e^{\mathrm{j}2\pi(f_c-f)\tau_{11,m_n}(t)} \mathbf{a}_{T,m_n}^H. \tag{3}$$

Here, $\mathbf{P}_{m_n}(t)$ is the $M_R \times M_T$ power matrix composed of the power of ray $P_{qp,m_n}(t)$, $P_{qp,m_n}(t)$ is the power of the ray from the antenna A_p^T through the mth scatterer in the nth cluster to the antenna A_q^R at time t, $\odot$ is the Hadamard multiplication based on elements, f_c is the carrier frequency, $\kappa_{m_n}(t)$ is the cross-polarization ratio, $\theta_L^{V_p V_p}$ and $\theta_L^{H_p H_p}$ are random phases of vertical polarization and horizontal polarization of the LoS component following a uniform distribution in $[0, 2\pi)$, respectively. Random phases of vertical polarization and horizontal polarization of the NLoS components following a uniform distribution in $[0, 2\pi)$ are expressed as $\theta_{m_n}^{V_p V_p}$ and $\theta_{m_n}^{H_p H_p}$, respectively. Random phases for the cross polarization of the NLoS components following a uniform distribution in $[0, 2\pi)$ are expressed as $\theta_{m_n}^{V_p H_p}$ and $\theta_{m_n}^{H_p V_p}$. The transpose and conjugate transpose operators are expressed as $(\cdot)^T$ and $(\cdot)^H$, respectively. The radiation patterns of the antenna elements with vertical polarization and horizontal polarization of the LoS component at the Tx side or the Rx side are expressed as $F_{V_p}\left(\phi_{E,L}^T(t), \phi_{A,L}^T(t)\right)$ and $F_{H_p}\left(\phi_{E,L}^T(t), \phi_{A,L}^T(t)\right)$ or $F_{V_p}\left(\phi_{E,L}^R(t), \phi_{A,L}^R(t)\right)$ and $F_{H_p}\left(\phi_{E,L}^R(t), \phi_{A,L}^R(t)\right)$, respectively. The radiation patterns of the antenna elements with vertical polarization and horizontal polarization of NLoS components at the Tx side or the Rx side are expressed as $F_{V_p}\left(\phi_{E,m_n}^T(t), \phi_{A,m_n}^T(t)\right)$ and $F_{H_p}\left(\phi_{E,m_n}^T(t), \phi_{A,m_n}^T(t)\right)$ or $F_{V_p}\left(\phi_{E,m_n}^R(t), \phi_{A,m_n}^R(t)\right)$ and $F_{H_p}\left(\phi_{E,m_n}^R(t), \phi_{A,m_n}^R(t)\right)$, respectively. Steering vectors of the LoS path and NLoS components at the Tx side are expressed as $\mathbf{a}_{T,L}(t)$ and $\mathbf{a}_{T,m_n}(t)$, respectively.

Steering vectors of the LoS path and NLoS components at the Rx side are expressed as $\mathbf{a}_{R,L}(t)$ and $\mathbf{a}_{R,m_n}(t)$, respectively [41], [42]. The power of the ray from the antenna A_1^T through the mth scatterer in the nth cluster to the antenna A_1^R at time t is denoted as $P_{11,m_n}(t)$. The delay from the antenna A_1^T to the antenna A_1^R at time t is $\tau_{11}^L(t)$. The delay from the antenna A_1^T through the mth scatterer in the nth cluster to the antenna A_1^R at time t is $\tau_{11,m_n}(t)$, which can be calculated as

$$\tau_{11,m_n}(t) = \frac{d_{11,m_n}(t)}{c} = \frac{\parallel \vec{d}_{1,m_n}^T(t) \parallel}{c} + \frac{\parallel \vec{d}_{1,m_n}^R(t) \parallel}{c} + \tilde{\tau}_{m_n}. \tag{4}$$

Here, c represents the speed of light, $\parallel \cdot \parallel$ represents the Euclidean norm operator, $d_{11,m_n}(t)$ is the distance from the antenna A_1^T through the mth scatterer in the nth cluster to the antenna A_1^R at time t, $\vec{d}_{1,m_n}^T(t)$ is the distance vector between the antenna A_1^T and the mth scatterer of the first bounce cluster C_n^A at time t, $\vec{d}_{1,m_n}^R(t)$ is the distance vector between the antenna A_1^R and the mth scatterer of the last bounce cluster C_n^Z at time t, and $\tilde{\tau}_{m_n}$ is the virtual delay from the first bounce cluster C_n^A at the Tx side to the last bounce cluster C_n^Z at the Rx side.

B. Spherical Wavefront

As an important channel characteristic of ultra-massive MIMO, the spherical wavefront needs to be considered in channel modeling. Thus, steering vectors at the Tx or Rx side are derived according to different Tx or Rx antennas and angles of departure or arrival. From Fig. 2 (a), we can see that different antennas have different angles and distances to the same reference source for the spherical wavefront. However, different antennas have the same angle for the plane wavefront, which is shown in Fig. 2 (b).

1) LoS: Steering vectors $\mathbf{a}_{T,L}(\phi_{E,L}^T, \phi_{A,L}^T, d_{1,L}^T)$ and $\mathbf{a}_{R,L}(\phi_{E,L}^R, \phi_{A,L}^R, d_{1,L}^R)$ of LoS component can be expressed as [43], [44]

$$\mathbf{a}_{T,L}(\phi_{E,L}^T, \phi_{A,L}^T, d_{1,L}^T) = \frac{1}{\sqrt{M_T}} \left[1, e^{\mathrm{j}2\pi \frac{d_{2,L}^T(t)-d_{1,L}^T(t)}{\lambda}}, \cdots, e^{\mathrm{j}2\pi \frac{d_{p,L}^T(t)-d_{1,L}^T(t)}{\lambda}}, \cdots, e^{\mathrm{j}2\pi \frac{d_{M_T,L}^T(t)-d_{1,L}^T(t)}{\lambda}} \right]^T \tag{5}$$

and

$$\mathbf{a}_{R,L}(\phi_{E,L}^R, \phi_{A,L}^R, d_{1,L}^R) = \frac{1}{\sqrt{M_R}} \left[1, e^{\mathrm{j}2\pi \frac{d_{2,L}^R(t)-d_{1,L}^R(t)}{\lambda}}, \cdots, e^{\mathrm{j}2\pi \frac{d_{q,L}^R(t)-d_{1,L}^R(t)}{\lambda}}, \cdots, e^{\mathrm{j}2\pi \frac{d_{M_R,L}^R(t)-d_{1,L}^R(t)}{\lambda}} \right]^T. \tag{6}$$

Here, $d_{1,L}^T(t)$, $d_{p,L}^T(t)$, $d_{1,L}^R(t)$, and $d_{q,L}^R(t)$ are the distances of LoS path from antenna A_1^T to A_1^R, A_p^T to A_1^R, A_1^R to A_1^T, and A_q^R to A_1^T at time t, respectively. The EAoD, AAoD, EAoA, and AAoA of LoS path at initial time are expressed as $\phi_{E,L}^T$, $\phi_{A,L}^T$, $\phi_{E,L}^R$, and $\phi_{A,L}^R$, respectively. The distances of LoS path from antenna A_1^T to A_1^R and A_1^R to A_1^T at initial time are expressed as $d_{1,L}^T$ and $d_{1,L}^R$, respectively.

2) NLoS: Similarly, steering vectors $\mathbf{a}_{T,m_n}(\phi_{E,m_n}^T, \phi_{A,m_n}^T, d_{1,m_n}^T)$ and $\mathbf{a}_{R,m_n}(\phi_{E,m_n}^R, \phi_{A,m_n}^R, d_{1,m_n}^R)$ of NLoS components for the mth ray of nth path can be expressed as

$$\mathbf{a}_{T,m_n}(\phi_{E,m_n}^T, \phi_{A,m_n}^T, d_{1,m_n}^T) =$$
$$\frac{1}{\sqrt{M_T}}\left[1, e^{j2\pi\frac{d_{2,m_n}^T(t)-d_{1,m_n}^T(t)}{\lambda}}, \cdots, e^{j2\pi\frac{d_{p,m_n}^T(t)-d_{1,m_n}^T(t)}{\lambda}}, \cdots, e^{j2\pi\frac{d_{M_T,m_n}^T(t)-d_{1,m_n}^T(t)}{\lambda}}\right]^T \quad (7)$$

and

$$\mathbf{a}_{R,m_n}(\phi_{E,m_n}^R, \phi_{A,m_n}^R, d_{1,m_n}^R) =$$
$$\frac{1}{\sqrt{M_R}}\left[1, e^{j2\pi\frac{d_{2,m_n}^R(t)-d_{1,m_n}^R(t)}{\lambda}}, \cdots, e^{j2\pi\frac{d_{q,m_n}^R(t)-d_{1,m_n}^R(t)}{\lambda}}, \cdots, e^{j2\pi\frac{d_{M_R,m_n}^R(t)-d_{1,m_n}^R(t)}{\lambda}}\right]^T. \quad (8)$$

Here, $d_{1,m_n}^T(t)$ or $d_{1,m_n}^R(t)$ and $d_{p,m_n}^T(t)$ or $d_{q,m_n}^R(t)$ are the distances of paths from antenna A_1^T or A_1^R and A_p^T or A_q^R to the mth scatterer in the nth cluster at the Tx or Rx side at time t, respectively. The EAoD and AAoD from antenna A_1^T to the mth scatterer in the nth cluster for
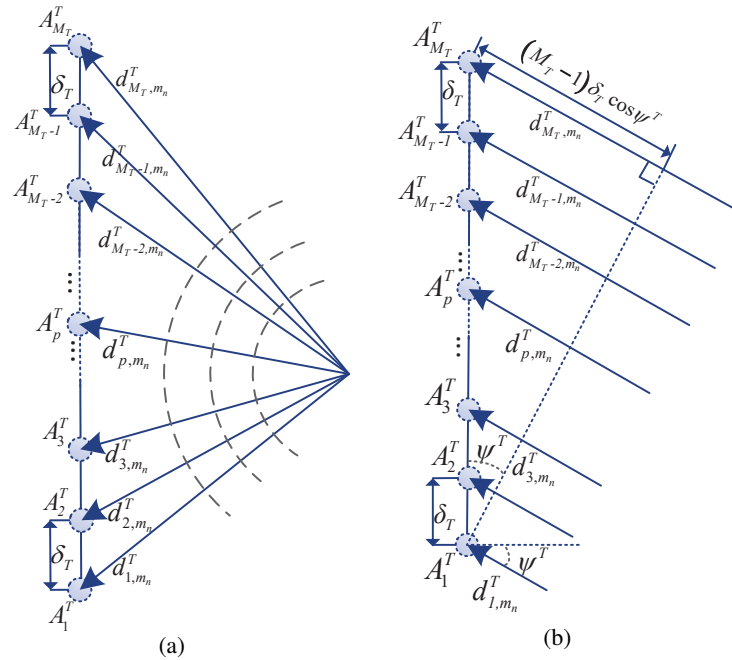
Fig. 2. Illustrations of (a) near-field spherical wavefront and (b) far-field plane wavefront.

the Tx at initial time are expressed as ϕ_{E,m_n}^T and ϕ_{A,m_n}^T, respectively. The EAoA and AAoA from antenna A_1^R to the mth scatterer in the nth cluster at the Rx at initial time are expressed as ϕ_{E,m_n}^R and ϕ_{A,m_n}^R, respectively. The distances from antenna A_1^T and A_1^R to the mth scatterer in the nth cluster for the Tx and Rx side at initial time are expressed as d_{1,m_n}^T and d_{1,m_n}^R, respectively. The phases are associated with distance differences when $d_{1,L}^T(t)$, $d_{1,L}^R(t)$, $d_{1,m_n}^T(t)$, and $d_{1,m_n}^R(t)$ are used as references according to (5)–(8).

For LoS and NLoS components, calculation methods of steering vectors are consistent. Thus, we take steering vectors of NLoS components as an example. To further derive $\mathbf{a}_{T,m_n}(\phi_{E,m_n}^T, \phi_{A,m_n}^T, d_{1,m_n}^T)$ and $\mathbf{a}_{R,m_n}(\phi_{E,m_n}^R, \phi_{A,m_n}^R, d_{1,m_n}^R)$, we firstly calculate vectors $\vec{d}_{p,m_n}^T(t)$ and $\vec{d}_{q,m_n}^R(t)$ as

$$\vec{d}_{p,m_n}^T(t) = \vec{d}_{1,m_n}^T + \int_0^t \vec{v}^{A_n}(t)dt - \int_0^t \vec{v}^T(t)dt - \vec{l}_p^T \tag{9}$$

and

$$\vec{d}_{q,m_n}^R(t) = \vec{d}_{1,m_n}^R + \int_0^t \vec{v}^{Z_n}(t)dt - \int_0^t \vec{v}^R(t)dt - \vec{l}_q^R \tag{10}$$

where $\vec{l}_p^T$ and $\vec{l}_q^R$ are vectors from A_1^T to A_p^T and A_1^R to A_q^R, respectively. After obtaining vectors $\vec{d}_{p,m_n}^T(t)$ and $\vec{d}_{q,m_n}^R(t)$, we can obtain vectors $\vec{d}_{1,m_n}^T(t)$ and $\vec{d}_{1,m_n}^R(t)$ by setting $p = 1$ and $q = 1$, respectively. Correspondingly, distance differences $d_{p,m_n}^T(t) - d_{1,m_n}^T(t)$ and $d_{q,m_n}^R(t) - d_{1,m_n}^R(t)$ can be obtained by higher-order Taylor expansion (see Appendix A). Then, steering vectors $\mathbf{a}_{T,m_n}(\phi_{E,m_n}^T, \phi_{A,m_n}^T, d_{1,m_n}^T)$ and $\mathbf{a}_{R,m_n}(\phi_{E,m_n}^R, \phi_{A,m_n}^R, d_{1,m_n}^R)$ can be further expressed as

$$\mathbf{a}_{T,m_n}\left(\phi_{E,m_n}^T, \phi_{A,m_n}^T, d_{1,m_n}^T\right) \approx \frac{1}{\sqrt{M_T}}\left[a_{T,m_n}^1, \cdots, a_{T,m_n}^p, \cdots, a_{T,m_n}^{M_T}\right]^T \tag{11}$$

and

$$\mathbf{a}_{R,m_n}(\phi_{E,m_n}^R, \phi_{A,m_n}^R, d_{1,m_n}^R) \approx \frac{1}{\sqrt{M_R}}\left[a_{R,m_n}^1, \cdots, a_{R,m_n}^q, \cdots, a_{R,m_n}^{M_R}\right]^T. \tag{12}$$

Note that we change the form of (7) and (8) to (11) and (12), respectively. Here, a_{T,m_n}^p and a_{R,m_n}^q can be expressed as

$$a_{T,m_n}^p = e^{j2\pi\lambda^{-1}\left[-(p-1)\delta_T \sin\Psi^T\right]}e^{j2\pi\lambda^{-1}\left[(p-1)^2\delta_T^2(2d_{1,m_n}^T)^{-1}\left(1-\sin^2\Psi^T\right)\right]}$$
$$e^{j2\pi\lambda^{-1}\left[-2(p-1)\delta_T v^T t(d_{1,m_n}^T)^{-1}\sin\Psi^T\left(1-\cos\Xi^T\right)\right]} \tag{13}$$

and

$$a_{R,m_n}^q = e^{j2\pi\lambda^{-1}\left[-(q-1)\delta_R \sin\Psi^R\right]}e^{j2\pi\lambda^{-1}\left[(q-1)^2\delta_R^2(2d_{1,m_n}^R)^{-1}\left(1-\sin^2\Psi^R\right)\right]}$$
$$e^{j2\pi\lambda^{-1}\left[-2(q-1)\delta_R v^R t(d_{1,m_n}^R)^{-1}\sin\Psi^R\left(1-\cos\Xi^R\right)\right]}. \tag{14}$$

Here, $\sin \Psi^T = \sin \phi_{E,m_n}^T \sin \beta_E^T + \cos \phi_{E,m_n}^T \cos \beta_E^T \cos \left(\phi_{A,m_n}^T - \beta_A^T \right)$, $\cos \Xi^T = \cos \phi_{E,m_n}^T \cos$ $\left(\phi_{A,m_n}^T - \alpha^T \right)$, $\sin \Psi^R = \sin \phi_{E,m_n}^R \sin \beta_E^R + \cos \phi_{E,m_n}^R \cos \beta_E^R \cos \left(\phi_{A,m_n}^R - \beta_A^R \right)$, and $\cos \Xi^R = \cos \phi_{E,m_n}^R \cos \left(\phi_{A,m_n}^R - \alpha^R \right)$. They have been derived in Appendix A. The relative speeds for the Tx and cluster C_n^A, and the Rx and cluster C_n^Z are expressed as v^T and v^R, respectively. Equations (11) and (12) are steering vectors in the near-field spherical wavefront condition. In the far-field plane wavefront condition, (11) and (12) can be further simplified as

$$
\mathbf{a}_{T,m_n}(\phi_{E,m_n}^T, \phi_{A,m_n}^T) = \frac{1}{\sqrt{M_T}} \left[1, e^{j2\pi\lambda^{-1}\left[-\delta_T \sin \Psi^T\right]}, \cdots, e^{j2\pi\lambda^{-1}\left[-(p-1)\delta_T \sin \Psi^T\right]}, \right.
$$
$$
\left. \cdots, e^{j2\pi\lambda^{-1}\left[-(M_T-1)\delta_T \sin \Psi^T\right]} \right]^T
\tag{15}
$$

and

$$
\mathbf{a}_{R,m_n}(\phi_{E,m_n}^R, \phi_{A,m_n}^R) = \frac{1}{\sqrt{M_R}} \left[1, e^{j2\pi\lambda^{-1}\left[-\delta_R \sin \Psi^R\right]}, \cdots, e^{j2\pi\lambda^{-1}\left[-(q-1)\delta_R \sin \Psi^R\right]}, \right.
$$
$$
\left. \cdots, e^{j2\pi\lambda^{-1}\left[-(M_R-1)\delta_R \sin \Psi^R\right]} \right]^T.
\tag{16}
$$

Note that phases of the steering vectors present non-linear relationships with antenna indices in the near-field spherical wavefront condition and linear relationships with antenna indices in the far-field plane wavefront condition. This reflects that the complexity of near-field spherical wavefront model is further increased compared to that of the far-field plane wavefront.

C. Spatial Non-stationarity

Another important channel characteristic of the ultra-massive MIMO is spatial non-stationarity. We consider the cluster birth-death process along the antenna array to model spatial non-stationarity. The detailed cluster birth-death process is the same as that in [13].

D. Channel Transfer Function (CTF) and Channel Impulse Response (CIR)

The CTF is the element of the channel matrix. After obtain the channel matrix, we can rewrite the CTF as

$$
H_{qp}^L(t,f) = \begin{bmatrix} F_{V_p}\left(\phi_{E,L}^R(t), \phi_{A,L}^R(t)\right) \\ F_{H_p}\left(\phi_{E,L}^R(t), \phi_{A,L}^R(t)\right) \end{bmatrix}^T \begin{bmatrix} e^{j\theta_L^{V_p V_p}} & 0 \\ 0 & -e^{j\theta_L^{H_p H_p}} \end{bmatrix} \begin{bmatrix} F_{V_p}\left(\phi_{E,L}^T(t), \phi_{A,L}^T(t)\right) \\ F_{H_p}\left(\phi_{E,L}^T(t), \phi_{A,L}^T(t)\right) \end{bmatrix}
$$
$$
\times e^{j2\pi(f_c-f)\tau_{qp}^L(t)}
\tag{17}
$$

and

$$H_{qp}^N(t,f) = \sum_{n=1}^{N(t)} \sum_{m=1}^{M_n(t)} \begin{bmatrix} F_{V_p}\big(\phi_{E,m_n}^R(t), \phi_{A,m_n}^R(t)\big) \\ F_{H_p}\big(\phi_{E,m_n}^R(t), \phi_{A,m_n}^R(t)\big) \end{bmatrix}^T \begin{bmatrix} e^{\mathrm{j}\theta_{mn}^{V_p V_p}} & \sqrt{\kappa_{m_n}^{-1}(t)}e^{\mathrm{j}\theta_{mn}^{V_p H_p}} \\ \sqrt{\kappa_{m_n}^{-1}(t)}e^{\mathrm{j}\theta_{mn}^{H_p V_p}} & e^{\mathrm{j}\theta_{mn}^{H_p H_p}} \end{bmatrix}$$

$$\times \begin{bmatrix} F_{V_p}\big(\phi_{E,m_n}^T(t), \phi_{A,m_n}^T(t)\big) \\ F_{H_p}\big(\phi_{E,m_n}^T(t), \phi_{A,m_n}^T(t)\big) \end{bmatrix} \sqrt{P_{qp,m_n}(t)}e^{\mathrm{j}2\pi(f_c-f)\tau_{qp,m_n}(t)}. \tag{18}$$

Taking the inverse Fourier transform of the CTF, we can obtain the CIR

$$h_{qp}^L(t,\tau) = \begin{bmatrix} F_{V_p}\big(\phi_{E,L}^R(t), \phi_{A,L}^R(t)\big) \\ F_{H_p}\big(\phi_{E,L}^R(t), \phi_{A,L}^R(t)\big) \end{bmatrix}^T \begin{bmatrix} e^{\mathrm{j}\theta_L^{V_p V_p}} & 0 \\ 0 & -e^{\mathrm{j}\theta_L^{H_p H_p}} \end{bmatrix} \begin{bmatrix} F_{V_p}\big(\phi_{E,L}^T(t), \phi_{A,L}^T(t)\big) \\ F_{H_p}\big(\phi_{E,L}^T(t), \phi_{A,L}^T(t)\big) \end{bmatrix}$$

$$\times e^{\mathrm{j}2\pi f_c \tau_{qp}^L(t)}\delta\big(\tau - \tau_{qp}^L(t)\big) \tag{19}$$

and

$$h_{qp}^N(t,\tau) = \sum_{n=1}^{N(t)} \sum_{m=1}^{M_n(t)} \begin{bmatrix} F_{V_p}\big(\phi_{E,m_n}^R(t), \phi_{A,m_n}^R(t)\big) \\ F_{H_p}\big(\phi_{E,m_n}^R(t), \phi_{A,m_n}^R(t)\big) \end{bmatrix}^T \begin{bmatrix} e^{\mathrm{j}\theta_{mn}^{V_p V_p}} & \sqrt{\kappa_{m_n}^{-1}(t)}e^{\mathrm{j}\theta_{mn}^{V_p H_p}} \\ \sqrt{\kappa_{m_n}^{-1}(t)}e^{\mathrm{j}\theta_{mn}^{H_p V_p}} & e^{\mathrm{j}\theta_{mn}^{H_p H_p}} \end{bmatrix}$$

$$\times \begin{bmatrix} F_{V_p}\big(\phi_{E,m_n}^T(t), \phi_{A,m_n}^T(t)\big) \\ F_{H_p}\big(\phi_{E,m_n}^T(t), \phi_{A,m_n}^T(t)\big) \end{bmatrix} \sqrt{P_{qp,m_n}(t)}e^{\mathrm{j}2\pi f_c \tau_{qp,m_n}(t)}\delta\big(\tau - \tau_{qp,m_n}(t)\big). \tag{20}$$

Here, the CIR is consist with that in [13].

III. THE ULTRA-MASSIVE MIMO BDCM

The BDCM can be obtained by the unitary transformation of the GBSM. To introduce the concept of beam, we change the form of (2) and (3). The LoS and NLoS components of the channel matrix of the GBSM can be rewritten as [27]

$$\mathbf{H}^L(t,f) = \sum_{q=1}^{M_R} \sum_{p=1}^{M_T} \sum_{L \in S_{r,q} \bigcap S_{t,p}} \mathbf{a}_{R,L} \begin{bmatrix} F_{V_p}\big(\phi_{E,L}^R(t), \phi_{A,L}^R(t)\big) \\ F_{H_p}\big(\phi_{E,L}^R(t), \phi_{A,L}^R(t)\big) \end{bmatrix}^T \begin{bmatrix} e^{\mathrm{j}\theta_L^{V_p V_p}} & 0 \\ 0 & -e^{\mathrm{j}\theta_L^{H_p H_p}} \end{bmatrix}$$

$$\times \begin{bmatrix} F_{V_p}\big(\phi_{E,L}^T(t), \phi_{A,L}^T(t)\big) \\ F_{H_p}\big(\phi_{E,L}^T(t), \phi_{A,L}^T(t)\big) \end{bmatrix} e^{\mathrm{j}2\pi(f_c-f)\tau_{11}^L(t)}\mathbf{a}_{T,L}^H \tag{21}$$

and

$$\mathbf{H}^N(t,f) = \sqrt{\mathbf{P}_{m_n}(t)} \odot \sum_{q=1}^{M_R} \sum_{p=1}^{M_T} \mathbf{a}_{R,q} \sum_{m_n \in S_{r,q} \bigcap S_{t,p}} \begin{bmatrix} F_{V_p}(\phi_{E,m_n}^R(t), \phi_{A,m_n}^R(t)) \\ F_{H_p}(\phi_{E,m_n}^R(t), \phi_{A,m_n}^R(t)) \end{bmatrix}^T$$

$$\times \begin{bmatrix} e^{\mathrm{j}\theta_{mn}^{V_p V_p}} & \sqrt{\kappa_{m_n}^{-1}(t)}e^{\mathrm{j}\theta_{mn}^{V_p H_p}} \\ \sqrt{\kappa_{m_n}^{-1}(t)}e^{\mathrm{j}\theta_{mn}^{H_p V_p}} & e^{\mathrm{j}\theta_{mn}^{H_p H_p}} \end{bmatrix} \begin{bmatrix} F_{V_p}(\phi_{E,m_n}^T(t), \phi_{A,m_n}^T(t)) \\ F_{H_p}(\phi_{E,m_n}^T(t), \phi_{A,m_n}^T(t)) \end{bmatrix} e^{\mathrm{j}2\pi(f_c-f)\tau_{11,m_n}(t)}\mathbf{a}_{T,p}^H. \tag{22}$$

Here, we introduce beam partitions $S_{t,p}$ and $S_{r,q}$. Specifically, $S_{t,p}$ and $S_{r,q}$ are the sets of all paths whose transmitting and receiving angles are close to angles $\tilde{\theta}_p$ and $\tilde{\theta}_q$, respectively [27], [41]. Here, $\tilde{\theta}_p$ and $\tilde{\theta}_q$ are virtual angles for the samples of transmitting and receiving physical angles [27], [41]. They can be calculated as $\tilde{\theta}_p = \frac{2p-1}{2M_T} - \frac{1}{2}(p = 1, 2, \cdots, M_T)$ and $\tilde{\theta}_q = \frac{2q-1}{2M_R} - \frac{1}{2}(q = 1, 2, \cdots, M_R)$. Note that

$$\cup_p S_{t,p} = \cup_q S_{r,q} = \cup_{p,q}(S_{t,p} \cap S_{r,q}) = \{1, 2, \cdots, m_n, \cdots, N(t)M_n(t)\}. \tag{23}$$

From (23), we can see that only MPCs belonging to beam partitions $S_{t,p}$ and $S_{r,q}$ can be added to the qth row and pth column element of the BDCM. In addition, the relationship between virtual angles and physical angles can be expressed as

$$\tilde{\theta}_p = \frac{\delta_T}{\lambda}\sin\left(\phi_{E,m_n}^T\right)\sin\beta_E^T + \frac{\delta_T}{\lambda}\cos\left(\phi_{E,m_n}^T\right)\cos\beta_E^T\cos\left(\phi_{A,m_n}^T - \beta_A^T\right), \quad m_n \in S_{t,p} \tag{24}$$

and

$$\tilde{\theta}_q = \frac{\delta_R}{\lambda}\sin\left(\phi_{E,m_n}^R\right)\sin\beta_E^R + \frac{\delta_R}{\lambda}\cos\left(\phi_{E,m_n}^R\right)\cos\beta_E^R\cos\left(\phi_{A,m_n}^R - \beta_A^R\right), \quad m_n \in S_{r,q}. \tag{25}$$

Note that $\tilde{\theta}_p$ and $\tilde{\theta}_q$ are samples in the beam domain for the Tx and Rx, respectively.

After obtaining steering vectors $\mathbf{a}_{T,p}$ and $\mathbf{a}_{R,q}$, we can obtain steering matrices $\mathbf{A}_T$ and $\mathbf{A}_R$

$$\mathbf{A}_T = \Big[\mathbf{a}_{T,1}(\phi_{E,m_n}^T, \phi_{A,m_n}^T, d_{1,m_n}^T), \cdots, \mathbf{a}_{T,p}(\phi_{E,m_n}^T, \phi_{A,m_n}^T, d_{1,m_n}^T) \cdots,$$
$$\mathbf{a}_{T,M_T}(\phi_{E,m_n}^T, \phi_{A,m_n}^T, d_{1,m_n}^T)\Big], \quad m_n \in S_{t,p} \tag{26}$$

and

$$\mathbf{A}_R = \Big[\mathbf{a}_{R,1}(\phi_{E,m_n}^R, \phi_{A,m_n}^R, d_{1,m_n}^R), \cdots, \mathbf{a}_{R,q}(\phi_{E,m_n}^R, \phi_{A,m_n}^R, d_{1,m_n}^R) \cdots,$$
$$\mathbf{a}_{R,M_R}(\phi_{E,m_n}^R, \phi_{A,m_n}^R, d_{1,m_n}^R)\Big], \quad m_n \in S_{r,q}. \tag{27}$$

Equations (26) and (27) are steering matrices in the near-field spherical wavefront condition. The dimensions of $\mathbf{A}_T$ and $\mathbf{A}_R$ are $M_T \times M_T$ and $M_R \times M_R$, respectively. Steering vectors $\mathbf{a}_{T,p}\left(\phi_{E,m_n}^T, \phi_{A,m_n}^T, d_{1,m_n}^T\right)$ and $\mathbf{a}_{R,q}(\phi_{E,m_n}^R, \phi_{A,m_n}^R, d_{1,m_n}^R)$ for columns of $\mathbf{A}_T$ and $\mathbf{A}_R$ can be further expressed as

$$\mathbf{a}_{T,p}\left(\phi_{E,m_n}^T, \phi_{A,m_n}^T, d_{1,m_n}^T\right) = \frac{1}{\sqrt{M_T}}\left[a_{T,m_n}^1, \cdots, a_{T,m_n}^p, \cdots, a_{T,m_n}^{M_T}\right]^T, \quad m_n \in S_{t,p} \tag{28}$$

and

$$\mathbf{a}_{R,q}(\phi_{E,m_n}^R, \phi_{A,m_n}^R, d_{1,m_n}^R) = \frac{1}{\sqrt{M_R}}\left[a_{R,m_n}^1, \cdots, a_{R,m_n}^q, \cdots, a_{R,m_n}^{M_R}\right]^T, \quad m_n \in S_{r,q}. \tag{29}$$

Note that (28) and (29) are the pth column and qth column steering vectors of steering matrices $\mathbf{A}_T$ and $\mathbf{A}_R$, respectively. They are related to virtual angles $\tilde{\theta}_p$ and $\tilde{\theta}_q$ for all the MPCs of the mth scatterer in the nth cluster belonging to beam partitions $S_{t,p}$ and $S_{r,q}$. This can be represented by $m_n \in S_{t,p}$ and $m_n \in S_{r,q}$. The phases of steering vectors at the Tx and Rx sides are related to angles $\sin \Psi^T$ and $\sin \Psi^R$, and distances d_{1,m_n}^T and d_{1,m_n}^R in the near-field spherical wavefront condition according to (13) and (14). When $v^T = 0$, $v^R = 0$, $\frac{1-\sin^2 \Psi^T}{2d_{1,m_n}^T} = \mathbf{C}_{\text{con}}^T$, and $\frac{1-\sin^2 \Psi^R}{2d_{1,m_n}^R} = \mathbf{C}_{\text{con}}^R$ [44], $\mathbf{A}_T$ and $\mathbf{A}_R$ become unitary matrices in the near-field spherical wavefront condition. Note that $\mathbf{C}_{\text{con}}^T$ and $\mathbf{C}_{\text{con}}^R$ represent constants, and they are illustrated in Fig. 3.

In addition, in the far-field plane wavefront condition, (26) and (27) can be simplified as

$$\mathbf{A}_T = \left[\mathbf{a}_{T,1}(\phi_{E,m_n}^T, \phi_{A,m_n}^T), \cdots, \mathbf{a}_{T,p}(\phi_{E,m_n}^T, \phi_{A,m_n}^T), \cdots, \mathbf{a}_{T,M_T}(\phi_{E,m_n}^T, \phi_{A,m_n}^T) \right],$$
$$m_n \in S_{t,p} \tag{30}$$

and

$$\mathbf{A}_R = \left[\mathbf{a}_{R,1}(\phi_{E,m_n}^R, \phi_{A,m_n}^R), \cdots, \mathbf{a}_{R,q}(\phi_{E,m_n}^R, \phi_{A,m_n}^R), \cdots, \mathbf{a}_{R,M_R}(\phi_{E,m_n}^R, \phi_{A,m_n}^R) \right],$$
$$m_n \in S_{r,q}. \tag{31}$$

Here, $\mathbf{A}_T$ and $\mathbf{A}_R$ are unitary matrices. For ULA, by sampling the angle and distance rings in the near-field spherical wavefront condition and in the far-field plane wavefront condition, $\mathbf{A}_T$ and $\mathbf{A}_R$ are unitary matrices. For any antenna configuration, $\mathbf{A}_T$ and $\mathbf{A}_R$ become asymptotically
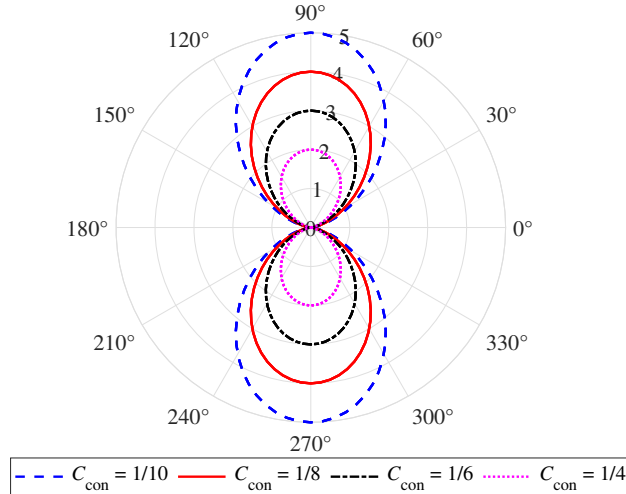
Fig. 3. Angle and distance rings $\left(\phi_{E,p}^T = 0, \beta_E^T = 0, \beta_A^T = 0, \phi_{A,p}^T \in [0,2\pi) \right)$.

unitary matrices when M_R and M_T tend to infinity [45]. The ultra-massive MIMO beam domain channel matrix $\mathbf{H}_b$ can be obtained as

$$\mathbf{H}_b(t,f) = \mathbf{A}_R \mathbf{H}(t,f) \mathbf{A}_T^H. \tag{32}$$

Here, beam domain channel matrix can be rewritten as

$$\mathbf{H}_b(t,f) = \sqrt{\frac{K_{RF}(t)}{K_{RF}(t)+1}} \mathbf{H}_b^L(t,f) + \sqrt{\frac{1}{K_{RF}(t)+1}} \mathbf{H}_b^N(t,f) \tag{33}$$

where $\mathbf{H}_b^L(t,f)$ and $\mathbf{H}_b^N(t,f)$ are LoS path and NLoS components of the beam domain channel matrix, respectively. Similarly, $\mathbf{H}_b(t,f)$, $\mathbf{H}_b^L(t,f)$, and $\mathbf{H}_b^N(t,f)$ are $M_R \times M_T$ matrices. Correspondingly, the qth row and pth column element of $\mathbf{H}_b^L(t,f)$ and $\mathbf{H}_b^N(t,f)$ can be expressed as [27], [41]

$$
\begin{aligned}
H_{b_q b_p}^L(t,f) \approx \sum_{L \in S_{r,q} \bigcap S_{t,p}} & \begin{bmatrix} F_{V_p}\big(\phi_{E,L}^R(t), \phi_{A,L}^R(t)\big) \\ F_{H_p}\big(\phi_{E,L}^R(t), \phi_{A,L}^R(t)\big) \end{bmatrix}^T \begin{bmatrix} e^{j\theta_L^{V_p V_p}} & 0 \\ 0 & -e^{j\theta_L^{H_p H_p}} \end{bmatrix} \\
& \times \begin{bmatrix} F_{V_p}\big(\phi_{E,L}^T(t), \phi_{A,L}^T(t)\big) \\ F_{H_p}\big(\phi_{E,L}^T(t), \phi_{A,L}^T(t)\big) \end{bmatrix} e^{j2\pi(f_c - f)\tau_{11}^L(t)}
\end{aligned}
\tag{34}
$$

and

$$
\begin{aligned}
H_{b_q b_p}^N(t,f) \approx \sum_{m_n \in S_{r,q} \bigcap S_{t,p}} & \begin{bmatrix} F_{V_p}(\phi_{E,m_n}^R(t), \phi_{A,m_n}^R(t)) \\ F_{H_p}(\phi_{E,m_n}^R(t), \phi_{A,m_n}^R(t)) \end{bmatrix}^T \begin{bmatrix} e^{j\theta_{m_n}^{V_p V_p}} & \sqrt{\kappa_{m_n}^{-1}(t)} e^{j\theta_{m_n}^{V_p H_p}} \\ \sqrt{\kappa_{m_n}^{-1}(t)} e^{j\theta_{m_n}^{H_p V_p}} & e^{j\theta_{m_n}^{H_p H_p}} \end{bmatrix} \\
& \times \begin{bmatrix} F_{V_p}(\phi_{E,m_n}^T(t), \phi_{A,m_n}^T(t)) \\ F_{H_p}(\phi_{E,m_n}^T(t), \phi_{A,m_n}^T(t)) \end{bmatrix} \sqrt{P_{m_n}(t)} e^{j2\pi(f_c - f)\tau_{11,m_n}(t)}.
\end{aligned}
\tag{35}
$$

Here, $P_{m_n}(t)$ is the power for the mth ray of nth path. Fig. 4 shows the beamwidth changing with different antenna numbers. We can see that with the increase of antenna numbers, the beamwidth becomes more and more narrow. This means the arrays can distinguish all angles of arrival and departure when the number of antennas approaches infinity.

IV. STATISTICAL PROPERTIES AND CHANNEL CAPACITIES OF THE GBSM AND BDCM

In this section, common statistical properties of the GBSM and the corresponding BDCM are studied and derived, including the STF correlation functions (CFs), SCCFs, TACFs, FCFs, normalized channel powers, and Doppler PSDs. Specific statistical properties such as the RMS angular spread of the GBSM and the RMS beam spread of the BDCM are derived. In addition, the channel capacities of the GBSM and the corresponding BDCM are studied and derived.
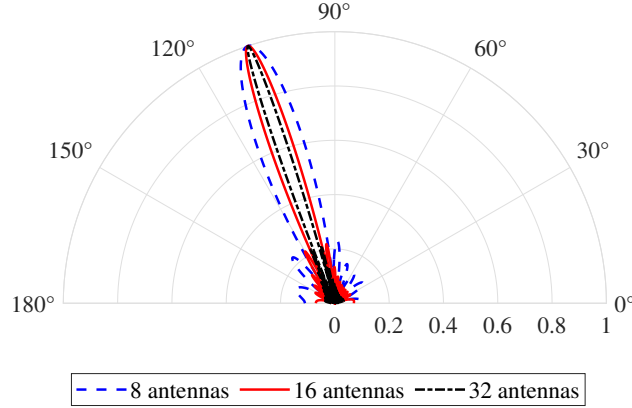
Fig. 4. The beamwidth with different antenna numbers.

A. STF CFs

STF CFs describe correlations of the GBSM and BDCM in the STF domains. After obtaining elements $H_{qp}(t, f)$ and $H_{q'p'}(t + \triangle t, f + \triangle f)$ of the channel matrix $\mathbf{H}(t, f)$, we can obtain the STF CF of the GBSM as

$$R_{qp,q'p'}(t, f; \triangle t, \triangle f) = E\left[H_{qp}(t, f)H^*_{q'p'}(t + \triangle t, f + \triangle f)\right] = \sqrt{\frac{K_{RF}(t)K_{RF}(t + \triangle t)}{\left(K_{RF}(t) + 1\right)\left(K_{RF}(t + \triangle t) + 1\right)}}$$

$$R^L_{qp,q'p'}(t, f; \triangle t, \triangle f) + \frac{1}{\sqrt{\left(K_{RF}(t) + 1\right)\left(K_{RF}(t + \triangle t) + 1\right)}} R^N_{qp,q'p'}(t, f; \triangle t, \triangle f) \qquad (36)$$

where $E[\cdot]$ is the expectation operator, $(\cdot)^*$ is the conjugate operator, $\triangle t$ is the time difference, $\triangle f$ is the frequency difference, p and p' represent different Tx antennas, q and q' represent different Rx antennas. The STF CFs of the LoS and NLoS components of the GBSM are $R^L_{qp,q'p'}(t, f; \triangle t, \triangle f)$ and $R^N_{qp,q'p'}(t, f; \triangle t, \triangle f)$, respectively. They can be further expressed as

$$R^L_{qp,q'p'}(t, f; \triangle t, \triangle f) = e^{j\frac{2\pi}{\lambda}\left[d^R_{q,L}(t) - d^R_{1,L}(t) - d^R_{q',L}(t + \triangle t) + d^R_{1,L}(t + \triangle t)\right]} e^{j\frac{2\pi}{\lambda f_c}(f_c - f)\left[d_L(t) - d_L(t + \triangle t)\right]}$$

$$\times\, e^{j\frac{2\pi}{\lambda f_c}\triangle f d_L(t + \triangle t)} e^{-j\frac{2\pi}{\lambda}\left[d^T_{p,L}(t) - d^T_{1,L}(t) - d^T_{p',L}(t + \triangle t) + d^T_{1,L}(t + \triangle t)\right]} \qquad (37)$$

and

$$R^N_{qp,q'p'}(t, f; \triangle t, \triangle f) = E\left[\sum_{n=1}^{N(t)}\sum_{m=1}^{M_n(t)}\sqrt{P_{qp,m_n}(t)P_{q'p',m_n}(t + \triangle t)}\right.$$

$$\times\, e^{j\frac{2\pi}{\lambda}\left[d^R_{q,m_n}(t) - d^R_{1,m_n}(t) - d^R_{q',m_n}(t + \triangle t) + d^R_{1,m_n}(t + \triangle t)\right]} e^{j\frac{2\pi}{\lambda f_c}(f_c - f)\left[d_{11,m_n}(t) - d_{11,m_n}(t + \triangle t)\right] + j\frac{2\pi}{\lambda f_c}\triangle f d_{11,m_n}(t + \triangle t)}$$

$$\left.\times\, e^{-j\frac{2\pi}{\lambda}\left[d^T_{p,m_n}(t) - d^T_{1,m_n}(t) - d^T_{p',m_n}(t + \triangle t) + d^T_{1,m_n}(t + \triangle t)\right]}\right]. \qquad (38)$$

Here, $d_L(t)$ represents the LoS distance between the antenna A^T_1 and the antenna A^R_1 at time t. Note that we consider omnidirectional single-polarized antennas for simplicity.

Similarly, when we obtain elements $H_{b_q b_p}(t, f)$ and $H_{b'_q b'_p}(t + \triangle t, f + \triangle f)$ of the channel matrix $\mathbf{H}_b(t, f)$, we can calculate the STF CF of the BDCM as

$$R_{b_q b_p, b'_q b'_p}(t, f; \triangle t, \triangle f) = E\left[H_{b_q b_p}(t, f)H^*_{b'_q b'_p}(t+\triangle t, f+\triangle f)\right] = \sqrt{\frac{K_{RF}(t)K_{RF}(t+\triangle t)}{\left(K_{RF}(t)+1\right)\left(K_{RF}(t+\triangle t)+1\right)}}$$

$$R^L_{b_q b_p, b'_q b'_p}(t, f; \triangle t, \triangle f) + \frac{1}{\sqrt{\left(K_{RF}(t) + 1\right)\left(K_{RF}(t + \triangle t) + 1\right)}} R^N_{b_q b_p, b'_q b'_p}(t, f; \triangle t, \triangle f). \tag{39}$$

Here, b_p and b'_p represent different Tx beams, b_q and b'_q represent different Rx beams. The STF CFs of LoS and NLoS components of the BDCM are $R^L_{b_q b_p, b'_q b'_p}(t, f; \triangle t, \triangle f)$ and $R^N_{b_q b_p, b'_q b'_p}(t, f; \triangle t, \triangle f)$, respectively. They can be expressed as

$$R^L_{b_q b_p, b'_q b'_p}(t, f; \triangle t, \triangle f) = E\left[\sum_{L\in S_{r,q}\bigcap S_{t,p}} \sum_{L'\in S_{r,q'}\bigcap S_{t,p'}} e^{\mathrm{j}\frac{2\pi}{\lambda f_c}(f_c-f)[d_L(t)-d_{L'}(t+\triangle t)]+\mathrm{j}\frac{2\pi}{\lambda f_c}\triangle f d_{L'}(t+\triangle t)}\right]$$

$$\tag{40}$$

and

$$R^N_{b_q b_p, b'_q b'_p}(t, f; \triangle t, \triangle f) = E\left[\sum_{m_n\in S_{r,q}\bigcap S_{t,p}} \sum_{m'_n\in S_{r,q'}\bigcap S_{t,p'}} \sqrt{P_{m_n}(t)P_{m_{n'}}(t + \triangle t)}\right.$$

$$\left. \times e^{\mathrm{j}\frac{2\pi}{\lambda f_c}(f_c-f)\left[d_{11,m_n}(t)-d_{11,m_{n'}}(t+\triangle t)\right]} e^{\mathrm{j}\frac{2\pi}{\lambda f_c}\triangle f d_{11,m'_n}(t+\triangle t)}\right]. \tag{41}$$

B. SCCFs

The SCCF of the GBSM describes the correlation of different antennas and can be expressed as

$$\gamma_{qp,q'p'}(t, f) = E\left[H_{qp}(t, f)H^*_{q'p'}(t, f)\right] = \frac{K_{RF}(t)}{K_{RF}(t) + 1}\gamma^L_{qp,q'p'}(t, f) + \frac{1}{K_{RF}(t) + 1}\gamma^N_{qp,q'p'}(t, f)$$

$$\tag{42}$$

where $\gamma^L_{qp,q'p'}(t, f)$ and $\gamma^N_{qp,q'p'}(t, f)$ are the SCCFs of LoS and NLoS components of the GBSM, respectively. They can be expressed as

$$\gamma^L_{qp,q'p'}(t, f) = e^{\mathrm{j}\frac{2\pi}{\lambda}\left[d^R_{q,L}(t)-d^R_{q',L}(t)-d^T_{p,L}(t)+d^T_{p',L}(t)\right]} \tag{43}$$

and

$$\gamma^N_{qp,q'p'}(t, f) = E\left[\sum_{n=1}^{N(t)}\sum_{m=1}^{M_n(t)} \sqrt{P_{qp,m_n}(t)P_{q'p',m_n}(t)} e^{\mathrm{j}\frac{2\pi}{\lambda}\left[d^R_{q,m_n}(t)-d^R_{q',m_n}(t)\right]} e^{\mathrm{j}\frac{2\pi}{\lambda}\left[-d^T_{p,m_n}(t)+d^T_{p',m_n}(t)\right]}\right]. \tag{44}$$

Note that the SCCF of the GBSM can also be obtained by setting $\triangle t = 0$ and $\triangle f = 0$ of the STF CF of the GBSM.

The SCCF of the BDCM describes the correlation of different beams and can be expressed as

$$\gamma_{b_q b_p, b'_q b'_p}(t, f) = E\left[H_{b_q b_p}(t, f)H^*_{b'_q b'_p}(t, f)\right] = \frac{K_{RF}(t)}{K_{RF}(t) + 1}\gamma^L_{b_q b_p, b'_q b'_p}(t, f)$$

$$+ \frac{1}{K_{RF}(t) + 1}\gamma^N_{b_q b_p, b'_q b'_p}(t, f). \tag{45}$$

In (45), $\gamma^L_{b_q b_p, b'_q b'_p}(t, f)$ and $\gamma^N_{b_q b_p, b'_q b'_p}(t, f)$ are the SCCFs of LoS and NLoS components of the BDCM, respectively. They can be expressed as

$$\gamma^L_{b_q b_p, b'_q b'_p}(t, f) = E\left[\sum_{L \in S_{r,q} \cap S_{t,p}} \sum_{L' \in S_{r,q'} \cap S_{t,p'}} e^{j\frac{2\pi}{\lambda f_c}(f_c - f)\left[d_L(t) - d_{L'}(t)\right]}\right] \tag{46}$$

and

$$\gamma^N_{b_q b_p, b'_q b'_p}(t, f) = E\left[\sum_{m_n \in S_{r,q} \cap S_{t,p}} \sum_{m'_n \in S_{r,q'} \cap S_{t,p'}} \sqrt{P_{m_n}(t)P_{m_{n'}}(t)} e^{j\frac{2\pi}{\lambda f_c}(f_c - f)\left[d_{11,m_n}(t) - d_{11,m_{n'}}(t)\right]}\right] \tag{47}$$

Similarly, the SCCF of the BDCM can also be obtained by setting $\triangle t = 0$ and $\triangle f = 0$ of the STF CF of the BDCM.

C. TACFs

The TACF of the GBSM describes the correlation of different time instants and can be expressed as

$$\zeta_{qp,qp}(t, f; \triangle t) = E\left[H_{qp}(t, f)H^*_{qp}(t + \triangle t, f)\right] = \sqrt{\frac{K_{RF}(t)K_{RF}(t + \triangle t)}{\left(K_{RF}(t) + 1\right)\left(K_{RF}(t + \triangle t) + 1\right)}}\zeta^L_{qp,qp}(t, f; \triangle t)$$

$$+ \frac{1}{\sqrt{\left(K_{RF}(t) + 1\right)\left(K_{RF}(t + \triangle t) + 1\right)}}\zeta^N_{qp,qp}(t, f; \triangle t) \tag{48}$$

where $\zeta^L_{qp,qp}(t, f; \triangle t)$ and $\zeta^N_{qp,qp}(t, f; \triangle t)$ are the TACFs of LoS and NLoS components of the GBSM, which can be expressed as

$$\zeta^L_{qp,qp}(t, f; \triangle t) = e^{j\frac{2\pi}{\lambda}\left[d^R_{q,L}(t) - d^R_{1,L}(t) - d^R_{q,L}(t + \triangle t) + d^R_{1,L}(t + \triangle t)\right]} e^{j\frac{2\pi}{\lambda f_c}(f_c - f)\left[d_L(t) - d_L(t + \triangle t)\right]}$$

$$\times e^{-j\frac{2\pi}{\lambda}\left[d^T_{p,L}(t) - d^T_{1,L}(t) - d^T_{p,L}(t + \triangle t) + d^T_{1,L}(t + \triangle t)\right]} \tag{49}$$

and

$$\zeta^N_{qp,qp}(t, f; \triangle t) = E\left[\sum_{n=1}^{N(t)} \sum_{m=1}^{M_n(t)} \sqrt{P_{qp,m_n}(t)P_{qp,m_n}(t + \triangle t)} e^{j\frac{2\pi}{\lambda f_c}(f_c - f)[d_{11,m_n}(t) - d_{11,m_n}(t + \triangle t)]}\right.$$

$$\times e^{j\frac{2\pi}{\lambda}\left[d^R_{q,m_n}(t) - d^R_{1,m_n}(t) - d^R_{q,m_n}(t + \triangle t) + d^R_{1,m_n}(t + \triangle t)\right]} e^{-j\frac{2\pi}{\lambda}\left[d^T_{p,m_n}(t) - d^T_{1,m_n}(t) - d^T_{p,m_n}(t + \triangle t) + d^T_{1,m_n}(t + \triangle t)\right]}\right] \tag{50}$$

Note that the TACF of the GBSM can also be obtained by setting $p = p'$, $q = q'$, and $\triangle f = 0$ of the STF CF of the GBSM.

Similarly, the TACF of the BDCM describes the correlation of different time instants and can be expressed as

$$\zeta_{b_q b_p, b_q b_p}(t, f; \triangle t) = E\left[H_{b_q b_p}(t, f) H_{b_q b_p}^*(t + \triangle t, f) \right] = \sqrt{\frac{K_{RF}(t) K_{RF}(t+\triangle t)}{\left(K_{RF}(t)+1 \right) \left(K_{RF}(t+\triangle t)+1 \right)}}$$

$$\zeta_{b_q b_p, b_q b_p}^{L}(t, f; \triangle t) + \frac{1}{\sqrt{\left(K_{RF}(t) + 1 \right) \left(K_{RF}(t + \triangle t) + 1 \right)}} \zeta_{b_q b_p, b_q b_p}^{N}(t, f; \triangle t). \tag{51}$$

Here, $\zeta_{b_q b_p, b_q b_p}^{L}(t, f; \triangle t)$ and $\zeta_{b_q b_p, b_q b_p}^{N}(t, f; \triangle t)$ are the TACFs of LoS and NLoS components of the BDCM, respectively. They can be expressed as

$$\zeta_{b_q b_p, b_q b_p}^{L}(t, f; \triangle t) = E\left[\sum_{L \in S_{r,q} \cap S_{t,p}} e^{j\frac{2\pi}{\lambda_{fc}}(f_c - f)\left[d_L(t) - d_L(t+\triangle t) \right]} \right] \tag{52}$$

and

$$\zeta_{b_q b_p, b_q b_p}^{N}(t, f; \triangle t) = E\left[\sum_{m_n \in S_{r,q} \cap S_{t,p}} \sqrt{P_{m_n}(t) P_{m_n}(t + \triangle t)} e^{j\frac{2\pi}{\lambda_{fc}}(f_c - f)\left[d_{11, m_n}(t) - d_{11, m_n}(t+\triangle t) \right]} \right] \tag{53}$$

The TACF of the BDCM can also be obtained by setting $b_p = b_p'$, $b_q = b_q'$, and $\triangle f = 0$ of the STF CF of the BDCM.

D. FCFs

The FCF of the GBSM describes the correlation of different carrier frequencies and can be expressed as

$$\kappa_{qp,qp}(t, f; \triangle f) = E\left[H_{qp}(t, f) H_{qp}^*(t, f; f + \triangle f) \right]$$
$$= \frac{K_{RF}(t)}{K_{RF}(t) + 1} \kappa_{qp,qp}^{L}(t, f; \triangle f) + \frac{1}{K_{RF}(t) + 1} \kappa_{qp,qp}^{N}(t, f; \triangle f) \tag{54}$$

where $\kappa_{qp,qp}^{L}(t, f; \triangle f)$ and $\kappa_{qp,qp}^{N}(t, f; \triangle f)$ are the FCFs of LoS and NLoS components of the GBSM, respectively. They can be expressed as

$$\kappa_{qp,qp}^{L}(t, f; \triangle f) = e^{j\frac{2\pi}{\lambda_{fc}}\triangle f d_L(t)} \tag{55}$$

and

$$\kappa_{qp,qp}^{N}(t, f; \triangle f) = E\left[\sum_{n=1}^{N(t)} \sum_{m=1}^{M_n(t)} P_{qp,m_n}(t) e^{j\frac{2\pi}{\lambda_{fc}}\triangle f d_{11, m_n}(t)} \right]. \tag{56}$$

The FCF of the GBSM can also be obtained by setting $p = p'$, $q = q'$, and $\triangle t = 0$ of the STF CF of the GBSM.

Similarly, the FCF of the BDCM describes the correlation of different carrier frequencies can be expressed as

$$\kappa_{b_q b_p, b_q b_p}(t, f; \triangle f) = E\left[H_{b_q b_p}(t, f)H^*_{b_q b_p}(t, f; f + \triangle f)\right] = \frac{K_{RF}(t)}{K_{RF}(t) + 1}\kappa^L_{b_q b_p, b_q b_p}(t, f; \triangle f)$$

$$+ \frac{1}{K_{RF}(t) + 1}\kappa^N_{b_q b_p, b_q b_p}(t, f; \triangle f). \tag{57}$$

Here, $\kappa^L_{b_q b_p, b_q b_p}(t, f; \triangle f)$ and $\kappa^N_{b_q b_p, b_q b_p}(t, f; \triangle f)$ are the FCFs of LoS and NLoS components of the BDCM, which can be expressed as

$$\kappa^L_{b_q b_p, b_q b_p}(t, f; \triangle f) = E\left[\sum_{L \in S_{r,q} \bigcap S_{t,p}} e^{j\frac{2\pi}{\lambda f_c}\triangle f d_L(t)}\right] \tag{58}$$

and

$$\kappa^N_{b_q b_p, b_q b_p}(t, f; \triangle f) = E\left[\sum_{m_n \in S_{r,q} \bigcap S_{t,p}} P_{m_n}(t)e^{j\frac{2\pi}{\lambda f_c}\triangle f d_{11,m_n}(t)}\right]. \tag{59}$$

The FCF of the BDCM can also be obtained by setting $b_p = b'_p$, $b_q = b'_q$, and $\triangle t = 0$ of the STF CF of the BDCM.

E. RMS Angular Spread and RMS Beam Spread

The RMS angular spread of the GBSM can be expressed as [46]

$$\phi_{as} = \left[\frac{\sum_{n=1}^{N}\sum_{m=1}^{M_n} P_{m_n}\left(\phi^R_{A,m_n}\right)^2}{\sum_{n=1}^{N}\sum_{m=1}^{M_n} P_{m_n}} - \left(\frac{\sum_{n=1}^{N}\sum_{m=1}^{M_n} P_{m_n}\phi^R_{A,m_n}}{\sum_{n=1}^{N}\sum_{m=1}^{M_n} P_{m_n}}\right)^2\right]^{1/2}. \tag{60}$$

The RMS beam spread of the BDCM can be expressed as

$$\phi_{bs} = \left[\frac{\sum_{q=1}^{M_R}\sum_{p=1}^{M_T}\sum_{m_n \in S_{r,q} \bigcap S_{t,p}} P_{m_n}\left(\phi^R_{A,m_n}\right)^2}{\sum_{q=1}^{M_R}\sum_{p=1}^{M_T}\sum_{m_n \in S_{r,q} \bigcap S_{t,p}} P_{m_n}} - \left(\frac{\sum_{q=1}^{M_R}\sum_{p=1}^{M_T}\sum_{m_n \in S_{r,q} \bigcap S_{t,p}} P_{m_n}\phi^R_{A,m_n}}{\sum_{q=1}^{M_R}\sum_{p=1}^{M_T}\sum_{m_n \in S_{r,q} \bigcap S_{t,p}} P_{m_n}}\right)^2\right]^{1/2} \tag{61}$$

F. Normalized Channel Powers

The normalized channel power of the GBSM can be expressed as

$$\tilde{P}(t, f) = \frac{\left|\mathbf{H}(t, f) \odot \mathbf{H}^H(t, f)\right|}{\max\left|\mathbf{H}(t, f) \odot \mathbf{H}^H(t, f)\right|} \tag{62}$$

where max represents the maximum element of the matrix and $|\cdot|$ represents the absolute value operator.

The normalized channel power of the BDCM can be expressed as

$$\tilde{P}_b(t, f) = \frac{\left|\mathbf{H}_b(t, f) \odot \mathbf{H}_b^H(t, f)\right|}{\max\left|\mathbf{H}_b(t, f) \odot \mathbf{H}_b^H(t, f)\right|}. \tag{63}$$

G. Doppler PSDs

The Doppler shift is caused by the movement of the UE. The Doppler PSD in the array domain can be defined as [38], [47], [48]

$$\psi(t, \nu, f) = \int E\left[H_{qp}(t, f)H_{qp}^*(t + \triangle t, f)\right] e^{-\mathrm{j}2\pi\nu\triangle t} d\triangle t \tag{64}$$

where $H_{qp}(t, f)$ is the element of the channel matrix $\mathbf{H}(t, f)$ and ν is the Doppler frequency.

Similarly, taking the Fourier transform of $E[H_{b_q b_p}(t, f)H_{b_q b_p}^*(t + \triangle t, f)]$ in the time domain, the Doppler PSD in the beam domain can be defined as [23]

$$\psi_b(t, \nu, f) = \int E[H_{b_q b_p}(t, f)H_{b_q b_p}^*(t + \triangle t, f)]e^{-\mathrm{j}2\pi\nu\triangle t} d\triangle t. \tag{65}$$

Here, $H_{b_q b_p}(t, f)$ is the element of the channel matrix $\mathbf{H}_b(t, f)$.

H. Channel Capacity

The channel capacity for communication to a single-user can be defined as [49], [50]

$$C = \frac{1}{N_s N_f} \sum_{s,f} \left[\log_2 \left[\det \left(\mathbf{I}_{M_R} + \frac{\rho}{M_T}\hat{\mathbf{H}}(s, f)\hat{\mathbf{H}}^H(s, f)\right)\right]\right] \tag{66}$$

where N_s is the number of snapshots, N_f is the number of frequency points, $\det[\cdot]$ is the determinant operator, ρ is the signal-to-noise ratio (SNR), $\mathbf{I}_{M_R}$ is the $M_R \times M_R$ identity matrix, and $\hat{\mathbf{H}}(s, f)$ is the normalized channel matrix for the sth snapshot and fth frequency point expressed as $\hat{\mathbf{H}}(s, f) = \mathbf{H}(s, f)/\sqrt{P_r(s, f)}$. Here, $P_r(s, f)$ is the received power for the sth snapshot and fth frequency point and can be obtained by $P_r(s, f) = \frac{1}{M_R M_T} \parallel \mathbf{H}(s, f) \parallel_{\mathrm{F}}^2$. Note that $\parallel \cdot \parallel_{\mathrm{F}}$ is the Frobenius norm operator.

V. RESULTS AND ANALYSIS

In this section, results and analysis of the GBSM and BDCM in the near-field and far-field conditions are studied, including SCCFs, TACFs, FCFs, RMS angular spread, RMS beam spread, level crossing rates (LCRs), average fading durations (AFDs) [51], etc. Non-stationary effects in the STF domains are demonstrated. Note that near-field and far-field conditions refer to the conditions of steering matrices transformed to unitary matrices rather than the actual near-field and far-field. By sampling the angle and distance rings, steering matrices of the spherical wavefront can be transformed to unitary matrices. In addition, steering matrices of the plane wavefront are unitary matrices. This achieves a perfect transformation from the GBSM to the

BDCM in the near-field and far-field conditions. The sparsity and insensitivity to Doppler shift and fading of the BDCM are also studied by the normalized channel power and Doppler PSD. In addition, channel capacities of the GBSM and BDCM in the near-field and far-field conditions are investigated.

A. Non-stationarity

1) SCCFs: SCCFs of the GBSM and BDCM are illustrated in Fig. 5. For the GBSM and BDCM, horizontal axes represent the antenna index and the beam index. The measurement data is taken from the ultra-massive channel measurement campaign, which is conducted at 5.3 GHz in a LoS environment [13]. We can see that simulation results of the GBSM in the near-field condition fit the measurement data well. This indicates that the GBSM is more accurate in the near-field condition than in the simplified far-field condition. In addition, the consistency of simulation results and analytical results illustrates the correctness of the GBSM and BDCM. The correlation of the BDCM is smaller compared with that of the GBSM, which indicates that the correlation in the beam domain is smaller than that in the array domain. Taking 0.5 as the threshold [13], the coherence distances can be obtained and they are smaller for the BDCM than those for the GBSM.

2) TACFs: As illustrated in Fig. 6, TACFs of the GBSM and BDCM are studied in near-field and for simplified far-field conditions. Both the Tx and Rx are equipped with ULAs. The number of Tx antennas M_T equals to 8 and the number of Rx antennas M_R equals to 128. The Tx is moving with a velocity of 2 m/s and the Rx is static. Similarly, the measurement data is taken from
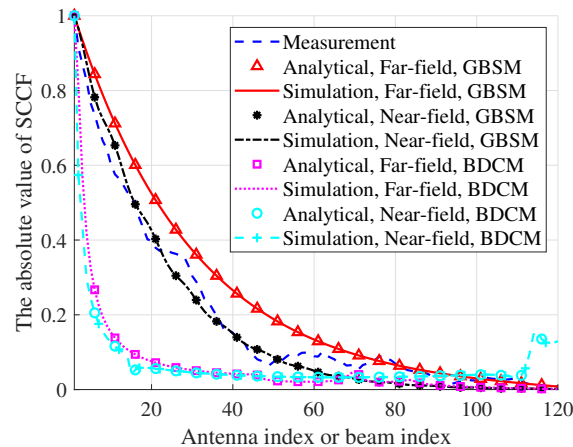
Fig. 5. SCCFs of the GBSM and BDCM in a LoS environment for Route 1, Position 6, ULA (f_c = 5.3 GHz, M_T = 8, M_R = 128, σ_{ASA} =σ_{ASD}= 5 m, σ_{ESA}= σ_{ESD} = 5 m, σ_{DS} = 4 m, λ^G = 20/m, λ^R = 1/m).
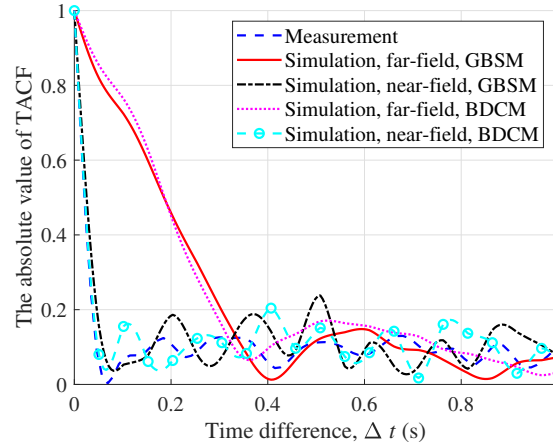
Fig. 6. TACFs of the GBSM and BDCM with the Tx moving along Route 1 (f_c = 5.3 GHz, M_T = 8, M_R = 128, σ_{ASA} = σ_{ASD}= 5 m, σ_{ESA} = σ_{ESD} = 5 m, σ_{DS} = 4 m, λ^G = 20/m, λ^R = 1/m, v^T = 2 m/s).

the ultra-massive channel measurement campaign, where the Tx is moving along Route 1 [13]. Simulation results of the GBSM and BDCM fit the measurement data well in the near-field condition, which indicates that the GBSM and BDCM are more accurate when considering the near-field effect than just making the far-field assumption. Correlations of the GBSM and BDCM are smaller considering near-field effect than those in the far-field case. In [52], the absolute value of the time-frequency correlation function for different antenna beamwidths shows that a smaller beamwidth leads to a larger correlation for the reduced number of clusters covered by antenna beams. Therefore, we can conclude that the simplified far-field effect discards some MPCs and reduces the accuracy in modeling near-field LoS environments.

3) FCFs: As shown in Fig. 7, FCFs of the GBSM and BDCM are studied in the near-field and simplified far-field conditions. Note that the antenna configuration and measurement environment are the same as those in Fig. 6. We can see that correlations of the GBSM and BDCM are smaller in the near-field condition than those in the far-field condition. This is because the far-field effect considers steering matrices only related to angle, which means fewer MPCs. The near-field effect considers steering matrices related to angle and distance, which covers more MPCs. Taking 0.5 as the threshold, the coherence bandwidths can be obtained and they are smaller for the GBSM and BDCM considering near-field effect than those in the far-field case.

4) RMS Angular Spread and RMS Beam Spread: Cumulative distribution functions (CDFs) of RMS angular spread of the GBSM and RMS beam spread of the BDCM in LoS environments are illustrated in Fig. 8. Note that the antenna configuration is the same as that in Fig. 6. We can see that simulation results of RMS angular spread of the GBSM and RMS beam spread of
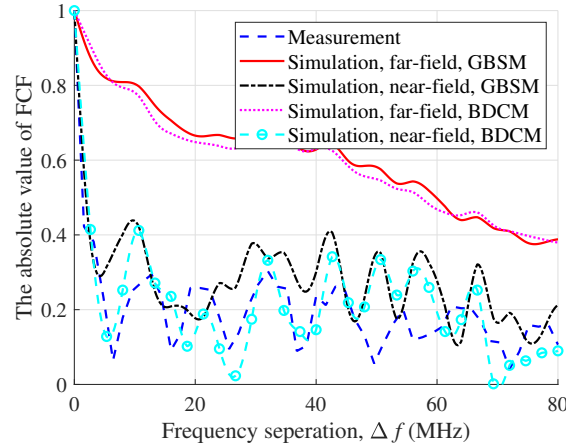
Fig. 7. FCFs of the GBSM and BDCM in a LoS environment for Route 1, Position 6, ULA (f_c = 5.3 GHz, M_T = 8, M_R = 128, $\sigma_{ASA} = \sigma_{ASD}$ = 5 m, $\sigma_{ESA} = \sigma_{ESD}$ = 5 m, σ_{DS} = 4 m, λ^G = 20/m, λ^R = 1/m).
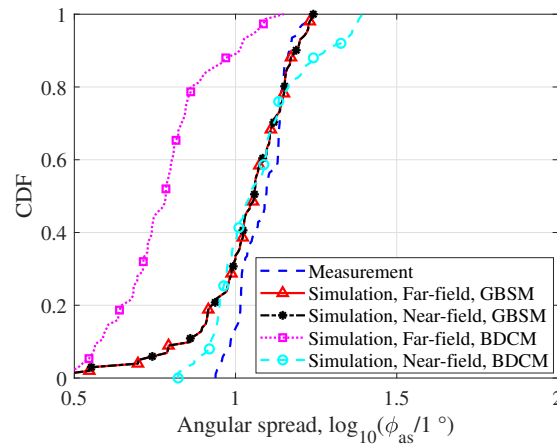
Fig. 8. The RMS angular spread of the GBSM and RMS beam spread of the BDCM in LoS environments (f_c = 5.3 GHz, M_T = 8, M_R = 128, $\sigma_{ASA} = \sigma_{ASD}$ = 7 m, $\sigma_{ESA} = \sigma_{ESD}$ = 5 m, σ_{DS} = 6 m, λ^G = 20/m, λ^R = 1/m).

the BDCM fit the measurement data well in the near-field condition. However, the simulation result for the RMS beam spread of the BDCM is smaller than the measurement data in the far-field condition. It is important to include near-field effects when modeling the performance of near-field propagation scenarios.

B. Beam Domain Sparsity

1) Normalized Channel Powers: Fig. 9 shows normalized channel powers of the GBSM and BDCM in a NLoS environment. Note that the antenna configuration is the same as that in Fig. 6. Compared with the normalized channel power of the GBSM, the normalized channel power of
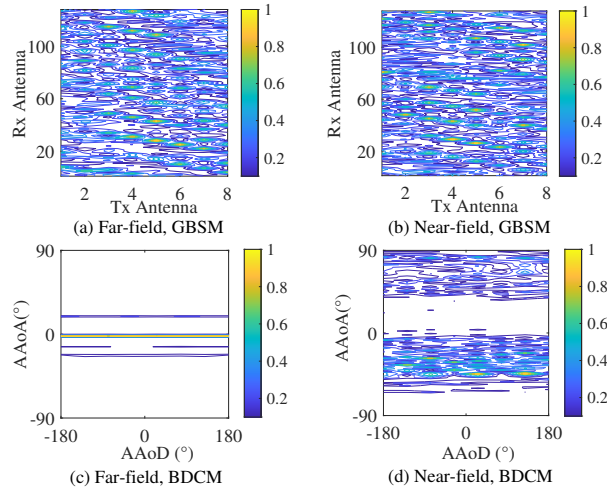
Fig. 9. Normalized channel powers in a NLoS environment (f_c = 5.3 GHz, M_T = 8, M_R = 128, σ_{ASA} = σ_{ASD} = 12 m, σ_{ESA} = σ_{ESD} = 10 m, σ_{DS} = 8 m, λ^G = 20/m, λ^R = 1/m).

the BDCM shows that most of the energy is contained at a few AAoAs, indicating the channel is spatially sparse. This is because that the GBSM superimposes all the MPCs in the array domain and the BDCM separates the MPCs of different angles by different beams. From Figs. 9 (c) and (d), the sparsity of the BDCM is more evident in the far-field condition than that in the near-field condition. Again, we can conclude that the near-field effect considers more MPCs than the far-field effect.

2) Doppler PSDs: Fig. 10 shows Doppler PSDs of the GBSM and BDCM. Again, the antenna configuration and measurement environment are the same as those in Fig. 6. Compared with the Doppler PSD of the GBSM, the Doppler PSD of the BDCM shows that most of the energy is contained at a few beams, indicating the channel is spatially sparse. Similarly, the sparsity of the BDCM is more evident in the far-field condition than that in the near-field condition, which also indicates that the near-field effect introduces more MPCs than far-field effect.

C. Beam Domain Insensitivity to Fading and Doppler Shift

1) Doppler PSDs: Fig. 11 (a) shows Doppler PSDs of the GBSM for antenna 1 and BDCM for beam 1 with the Tx moving along Route 1. The Doppler PSD of the BDCM is smaller than that of the GBSM. Compared with the Doppler PSD of the GBSM, there is no apparent peak for the Doppler PSD of the BDCM. This indicates that the BDCM illustrates insensitivity to Doppler shift. Fig. 11 (b) shows the CDFs of the Doppler PSD of the GBSM for antenna 1 and BDCM for beam 1 with the Tx moving along Route 1. The power of the BDCM for beam 1 is
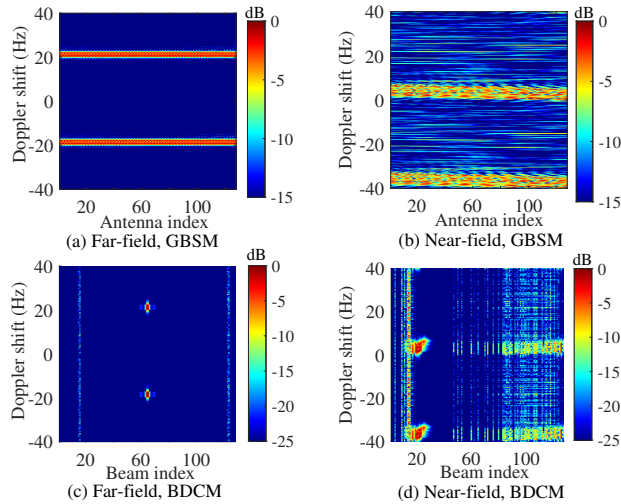
Fig. 10. Doppler PSDs of the GBSM and BDCM with the Tx moving along Route 1 (f_c = 5.3 GHz, M_T = 8, M_R = 128, σ_{ASA} = σ_{ASD} = 5 m, σ_{ESA} = σ_{ESD} = 5 m, σ_{DS} = 4 m, λ^G = 20/m, λ^R = 1/m, v^T = 2 m/s).
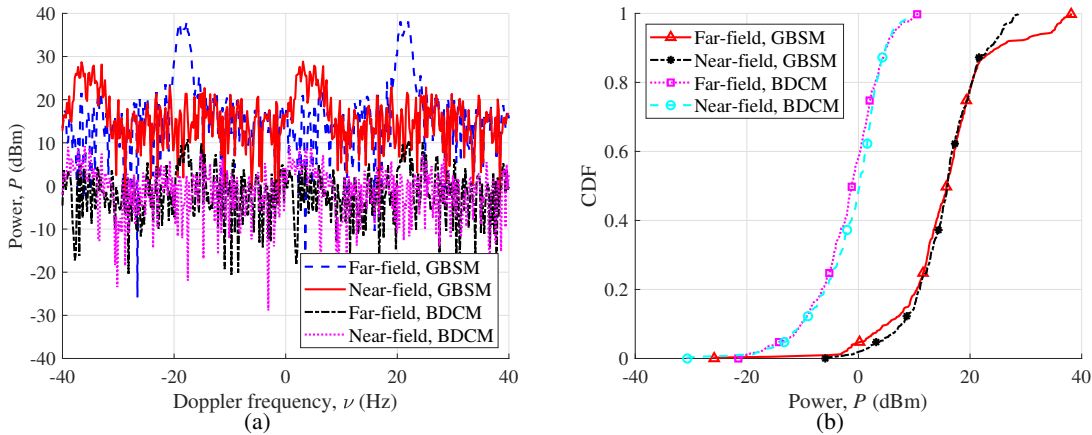
Fig. 11. Doppler PSDs of the GBSM for antenna 1 and BDCM for beam 1 with the Tx moving along Route 1.

much smaller than that of the GBSM for antemma 1. The corresponding MPCs of the BDCM for beam 1 cannot be estimated. This indicates that the BDCM shows insensitivity to fading than the GBSM. Figs. 12 (a) and (b) show the LCR and AFD of the amplitudes of GBSM for antenna 1 and BDCM for beam 1 with the Tx moving along Route 1. The reference level has a lot of influence on the LCR and AFD. The larger LCR brings the smaller AFD. In addition, the LCRs are larger in the near-field condition than those in the far-field condition for the GBSM and BDCM. The AFDs are smaller in the near-field condition than those in the far-field condition for the GBSM and BDCM.

D. Channel Capacity

As illustrated in Fig. 13, measured and simulated channel capacities of the GBSM and BDCM in LoS and NLoS environments are compared. The channel capacities of the GBSM and BDCM fit the measurement data better in the near-field condition than those in the far-field condition in LoS environments. However, the channel capacities of the GBSM and BDCM fit the
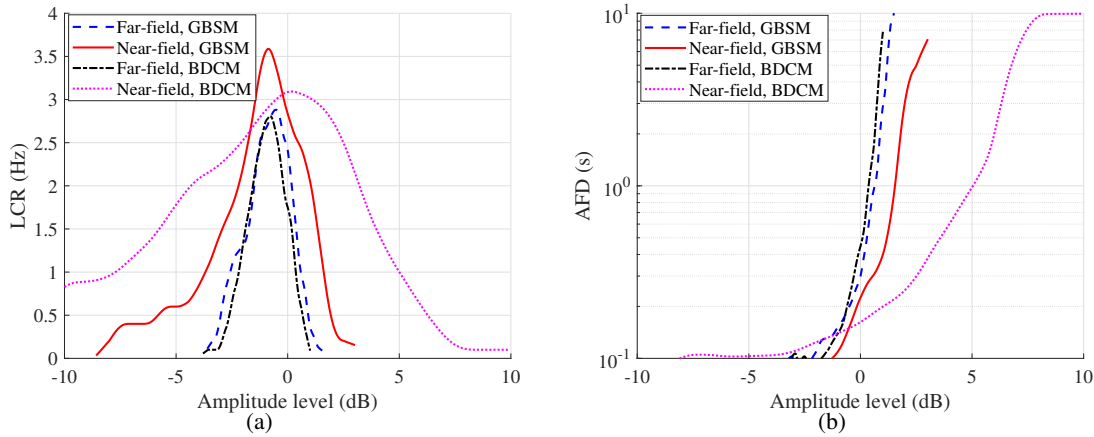
Fig. 12. The (a) LCRs and (b) AFDs of the amplitude of GBSM for antenna 1 and BDCM for beam 1 with the Tx moving along Route 1.
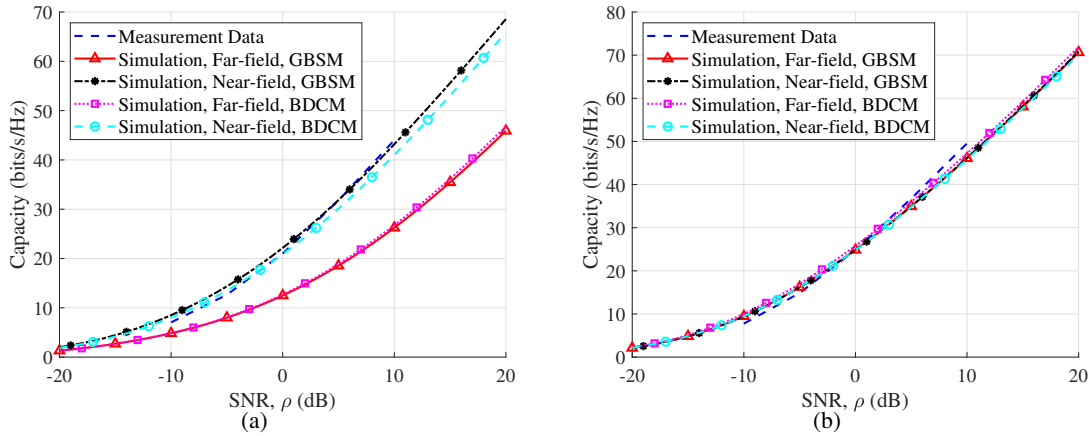
Fig. 13. Measured and simulated channel capacities in (a) LoS and (b) NLoS environments. (a) Measured and simulated channel capacities of a single-user in a LoS environment for Route 1, Position 7 (f_c = 5.3 GHz, M_T = 8, M_R = 128, $\sigma_{ASA} = \sigma_{ASD}$ = 7 m, $\sigma_{ESA} = \sigma_{ESD}$ = 5 m, σ_{DS} = 4 m, λ^G = 20/m, λ^R = 1/m). (b) Measured and simulated channel capacities of a single-user in a NLoS environment for Route 1, Position 1 (f_c = 5.3 GHz, M_T = 8, M_R = 128, $\sigma_{ASA} = \sigma_{ASD}$ = 12 m, $\sigma_{ESA} = \sigma_{ESD}$ = 10 m, σ_{DS} = 8 m, λ^G = 20/m, λ^R = 1/m).

measurement data well in both near-field and far-field conditions in NLoS environments. Again, the measurement data is from the single-user channel measurement campaign in [13]. We can conclude that near-field communications can improve system performance in LoS environments. However, near-field communications do not play an important influence on improving system performance in NLoS environments. This is because the near-field effect mainly increases the degrees of freedom (DoF) [53], [54] in LoS environments. In addition, as expected the channel capacities increase as the SNR increases.

VI. CONCLUSIONS

In this paper, an ultra-massive MIMO BDCM has been obtained by the transformation of the existing GBSM considering steering matrices of spherical wavefront and plane wavefront. Common statistical properties of the GBSM and BDCM have been investigated, including SCCFs, TACFs, FCFs, etc. Specific statistical properties, including the RMS angular spread of the GBSM and the RMS beam spread of the BDCM, have also been studied. Compared to the far-field condition, the near-field condition depends not only on distance but also on angle. This makes the correlations of the GBSM and BDCM lower in the near-field condition than those in the far-field condition for TACFs and FCFs. After the beam division, the correlation between different beams can be reduced. Thus, the correlation of BDCM is lower than that of the GBSM for SCCFs in both near-field and far-field conditions. The BDCM shows higher sparsity in the beam domain than the GBSM in the array domain, which provides a new view of beam domain for channel characteristic analysis to reduce the model complexity. In addition, the BDCM illustrates insensitivity to both Doppler shift and fading. Channel capacities results show that the near-field effect increases channel capacities in LoS environments. In conclusion, near-field communications may play an important role for higher frequencies and larger bandwidths in LoS environments.

APPENDIX A

THE DERIVATION OF $d_{p,m_n}^T(t) - d_{1,m_n}^T(t)$ AND $d_{q,m_n}^R(t) - d_{1,m_n}^R(t)$

The vectors in (9) can be expressed as

$$\vec{d}_{1,m_n}^T = d_{1,m_n}^T \left[\cos\phi_{E,m_n}^T \cos\phi_{A,m_n}^T, \cos\phi_{E,m_n}^T \sin\phi_{A,m_n}^T, \sin\phi_{E,m_n}^T \right] \tag{67}$$

$$\vec{v}^{A_n}(t) = v^{A_n}(t) \left[\cos\alpha_E^{A_n}(t) \cos\alpha_A^{A_n}(t), \cos\alpha_E^{A_n}(t) \sin\alpha_A^{A_n}(t), \sin\alpha_E^{A_n}(t) \right] \tag{68}$$

$$\vec{v}^T(t) = v^T(t) \left[\cos \alpha_E^T(t) \cos \alpha_A^T(t), \cos \alpha_E^T(t) \sin \alpha_A^T(t), \sin \alpha_E^T(t) \right] \tag{69}$$

and

$$\vec{l}_p^T = \delta_p \left[\cos \beta_E^T \cos \beta_A^T, \cos \beta_E^T \sin \beta_A^T, \sin \beta_E^T \right]. \tag{70}$$

Applying the vector rule of calculation and in the condition $\vec{v}^T(t) - \vec{v}^{A_n}(t) = v^T e^{j\alpha^T}$, we obtain distances $d_{p,m_n}^T(t) = \| \vec{d}_{p,m_n}^T(t) \|$ and $d_{1,m_n}^T(t) = \| \vec{d}_{1,m_n}^T(t) \|$ by higher-order Taylor expansion

$$d_{p,m_n}^T(t) \approx d_{1,m_n}^T - \delta_p \left[\sin \phi_{E,m_n}^T \sin \beta_E^T + \cos \phi_{E,m_n}^T \cos \beta_E^T \cos \left(\phi_{A,m_n}^T - \beta_A^T \right) \right] - v^T t \cos \phi_{E,m_n}^T$$
$$\cos \left(\phi_{A,m_n}^T - \alpha^T \right) + \frac{1}{2d_{1,m_n}^T} \left[\delta_p^2 \left(1 - \left(\sin \phi_{E,m_n}^T \sin \beta_E^T + \cos \phi_{E,m_n}^T \cos \beta_E^T \cos \left(\phi_{A,m_n}^T - \beta_A^T \right) \right)^2 \right) \right.$$
$$+ \left(v^T t \right)^2 \left(1 - \left(\cos \phi_{E,m_n}^T \cos \left(\phi_{A,m_n}^T - \alpha^T \right) \right)^2 \right) - 2\delta_p v^T t \left(\sin \phi_{E,m_n}^T \sin \beta_E^T + \cos \phi_{E,m_n}^T \right.$$
$$\left. \cos \beta_E^T \cos \left(\phi_{A,m_n}^T - \beta_A^T \right) \right) \left(1 - \cos \phi_{E,m_n}^T \cos \left(\phi_{A,m_n}^T - \alpha^T \right) \right) \right] \tag{71}$$

and

$$d_{1,m_n}^T(t) \approx d_{1,m_n}^T - v^T t \cos \phi_{E,m_n}^T \cos \left(\phi_{A,m_n}^T - \alpha^T \right) +$$
$$\frac{1}{2d_{1,m_n}^T} \left[\left(v^T t \right)^2 \left(1 - \cos \phi_{E,m_n}^T \cos \left(\phi_{A,m_n}^T - \alpha^T \right) \right)^2 \right]. \tag{72}$$

Thus, distance differences at the Tx side can be further expressed as

$$d_{p,m_n}^T(t) - d_{1,m_n}^T(t) = -\delta_p \left[\sin \phi_{E,m_n}^T \sin \beta_E^T + \cos \phi_{E,m_n}^T \cos \beta_E^T \cos \left(\phi_{A,m_n}^T - \beta_A^T \right) \right] + \frac{1}{2d_{1,m_n}^T}$$
$$\left[\delta_p^2 \left(1 - \left(\sin \phi_{E,m_n}^T \sin \beta_E^T + \cos \phi_{E,m_n}^T \cos \beta_E^T \cos \left(\phi_{A,m_n}^T - \beta_A^T \right) \right)^2 \right) - 2\delta_p v^T t \left(\sin \phi_{E,m_n}^T \right. \right.$$
$$\left. \sin \beta_E^T + \cos \phi_{E,m_n}^T \cos \beta_E^T \cos \left(\phi_{A,m_n}^T - \beta_A^T \right) \right) \left(1 - \cos \phi_{E,m_n}^T \cos \left(\phi_{A,m_n}^T - \alpha^T \right) \right) \right]. \tag{73}$$

For simplicity, we define $\sin \Psi^T$ and $\cos \Xi^T$ as

$$\sin \Psi^T = \sin \phi_{E,m_n}^T \sin \beta_E^T + \cos \phi_{E,m_n}^T \cos \beta_E^T \cos \left(\phi_{A,m_n}^T - \beta_A^T \right) \tag{74}$$

and

$$\cos \Xi^T = \cos \phi_{E,m_n}^T \cos \left(\phi_{A,m_n}^T - \alpha^T \right). \tag{75}$$

Applying $\delta_p = (p-1)\delta_T$ and substituting (75) into (73), we can obtain distance differences at the Tx side

$$d_{p,m_n}^T(t) - d_{1,m_n}^T(t) = \left[-(p-1)\,\delta_T \sin \Psi^T + \frac{(p-1)^2\,\delta_T^2}{2d_{1,m_n}^T} \left(1 - \sin^2 \Psi^T \right) \right.$$
$$\left. -\frac{2\,(p-1)}{d_{1,m_n}^T} \delta_T v^T t \sin \Psi^T \left(1 - \cos \Xi^T \right) \right]. \tag{76}$$

Similarly, distance differences at the Rx side can be expressed as

$$
\begin{aligned}
d_{q,m_n}^R(t) - d_{1,m_n}^R(t) = \Big[&-(q-1)\,\delta_R \sin \Psi^R + \frac{(q-1)^2 \delta_R^2}{2d_{1,m_n}^R} \left(1 - \sin^2 \Psi^R\right) \\
&- \frac{2(q-1)}{d_{1,m_n}^R} \delta_R v^R t \sin \Psi^R \left(1 - \cos \Xi^R\right) \Big].
\end{aligned}
\tag{77}
$$

REFERENCES

[1] C.-X. Wang, J. Huang, H. Wang, X.-Q. Gao, X.-H. You, and Y. Hao, "6G wireless channel measurements and models: Trends and challenges," *IEEE Veh. Technol. Mag.*, vol. 15, no. 4, pp. 22–32, Dec. 2020.

[2] C.-X. Wang, X.-H. You, X.-Q. Gao, *et al.*, "On the road to 6G: Visions, requirements, key technologies and testbeds," *IEEE Commun. Surveys Tuts.*, vol. 25, no. 2, pp. 905–974, 2nd Quart., 2023.

[3] E. Björnson, E. G. Larsson, and T. L. Marzetta, "Massive MIMO: Ten myths and one critical question," *IEEE Commun. Mag.*, vol. 54, no. 2, pp. 114–123, Feb. 2016.

[4] E. G. Larsson, F. Tufvesson, O. Edfors, and T. L. Marzetta, "Massive MIMO for next generation wireless systems," *IEEE Commun. Mag.*, vol. 52, no. 2, pp. 186–195, Feb. 2014.

[5] F. Rusek, D. Persson, B. K. Lau, E. G. Larsson, T. L. Marzetta, O. Edfors, and F. Tufvesson, "Scaling up MIMO: Opportunities and challenges with very large arrays," *IEEE Signal Proces. Mag.*, vol. 30, no. 1, pp. 40–46, Jan. 2013.

[6] L. Dai, J. Tan, Z. Chen, and H. V. Poor, "Delay-phase precoding for wideband THz massive MIMO," *IEEE Trans. Wireless Commun.*, vol. 21, no. 9, pp. 7271-7286, Sept. 2022.

[7] K. Zheng, S. Ou, and X. Yin, "Massive MIMO channel models: A survey," *Int. J. Antennas Propag.*, vol. 2014, no. 11, pp. 1–10, June 2014.

[8] W. Shen, L. Dai, Y. Zhang, J. Li, and Z. Wang, "On the performance of channel-statistics-based codebook for massive MIMO channel feedback," *IEEE Trans. Veh. Technol.*, vol. 66, no. 8, pp. 7553-7557, Aug. 2017.

[9] S. Payami and F. Tufvesson, "Channel measurements and analysis for very large array systems at 2.6 GHz," in *Proc. EUCAP'12*, Prague, Czech Republic, Mar. 2012, pp. 433–437.

[10] S. Payami and F. Tufvesson, "Delay spread properties in a measured massive MIMO system at 2.6 GHz," in *Proc. PIMRC'13*, London, UK, Sept. 2013, pp. 53–57.

[11] Y. Lu, C. Tao, and L. Liu, "Research on propagation characteristics of massive MIMO channel at 1.4725 GHz," in *Proc. IEEE VTC-Spring*, Sydney, NSW, Australia, June 2017, pp. 1–5.

[12] W. Li, L. Liu, C. Tao, Y. Lu, J. Xiao, and P. Liu, "Channel measurements and angle estimation for massive MIMO systems in a stadium," in *Proc. ICACT'15*, PyeongChang, Korea (South), July 2015, pp. 105–108.

[13] Y. Zheng, C.-X. Wang, R. Yang, L. Yu, F. Lai, J. Huang, R. Feng, C. Wang, C. Li, and Z. Zhong, "Ultra-massive MIMO channel measurements at 5.3 GHz and a general 6G channel model," *IEEE Trans. Veh. Technol.*, vol. 72, no. 1, pp. 20–34, Jan. 2023.

[14] Y. Zheng, C.-X. Wang, J. Huang, and R. Feng, "Channel measurements and analysis of 6G ultra-massive MIMO with different antenna configurations and scenarios," *IEEE Trans. Veh. Technol.*, early access, 2023, doi: 10.1109/TVT.2023.3258456.

[15] C.-X. Wang, J. Bian, J. Sun, W. Zhang, and M. Zhang, "A survey of 5G channel measurements and models," *IEEE Commun. Surveys Tuts.*, vol. 20, no. 4, pp. 3142–3168, 4th Quart. 2018.

[16] R. Feng, C.-X. Wang, J. Huang, and X. Gao, "Recent advances of ultramassive multiple-input, multiple-output technologies: Realizing a sixth-generation future in spatial and beam domains," *IEEE Veh. Technol. Mag.*, vol. 18, no. 1, pp. 70–79, Mar. 2023.

[17] R. Feng, C.-X. Wang, J. Huang, X.-Q. Gao, S. Salous, and H. Haas, "Classification and comparison of massive MIMO propagation channel models," *IEEE Int. Things J.*, vol. 9, no. 23, pp. 23452–23471, Dec. 2022.

[18] S. Wu, C.-X. Wang, E. H. M. Aggoune, M. M. Alwakeel, and Y. He, "A non-stationary 3-D wideband twin-cluster model for 5G massive MIMO channels," *IEEE J. Sel. Areas Commun.*, vol. 32, no. 6, pp. 1207–1218, June 2014.

[19] Y. Yuan, R. He, B. Ai, *et al.*, "A 3D geometry-based THz channel model for 6G ultra massive MIMO systems," *IEEE Trans. Veh. Technol.*, vol. 71, no. 3, pp. 2251-2266, Mar. 2022.

[20] J. Wang, C.-X. Wang, J. Huang, H. Wang, and X.-Q. Gao, "A general 3D space-time-frequency non-stationary THz channel model for 6G ultra-massive MIMO wireless communication systems," *IEEE J. Sel. Areas Commun.*, vol. 39, no. 6, pp. 1576–1589, June 2021.

[21] C. F. López and C.-X. Wang, "Novel 3D non-stationary wideband models for massive MIMO channels," *IEEE Trans. Wireless Commun.*, vol. 17, no. 5, pp. 2893–2905, May 2018.

[22] S. Wu, C.-X. Wang, e. H. M. Aggoune, M. M. Alwakeel, and X.-H. You, "A general 3D non-stationary 5G wireless channel model," *IEEE Trans. Commun.*, vol. 66, no. 7, pp. 3065–3078, July 2018.

[23] J. Bian, C.-X. Wang, X.-Q. Gao, X.-H. You, and M. Zhang, "A general 3D non-stationary wireless channel model for 5G and beyond," *IEEE Trans. Wireless Commun.*, vol. 20, no. 5, pp. 3211–3224, May 2021.

[24] L. You, X.-Q. Gao, G. Y. Li, X. Xia, and N. Ma, "BDMA for millimeter-wave/terahertz massive MIMO transmission with per-beam synchronization," *IEEE J. Sel. Areas Commun.*, vol. 35, no. 7, pp. 1550–1563, July 2017.

[25] F. Zhu, F. Gao, H. Lin, S. Jin, J. Zhao, and G. Qian, "Robust downlink beamforming for BDMA massive MIMO system," *IEEE Trans. Commun.*, vol. 66, no. 4, pp. 1496–1507, Apr. 2018.

[26] F. Zhu, F. Gao, H. Lin, S. Jin, J. Zhao, and G. Qian, "Robust beamforming for physical layer security in BDMA massive MIMO," *IEEE J. Sel. Areas Commun.*, vol. 36, no. 4, pp. 775-787, Apr. 2018.

[27] C. Sun, X.-Q. Gao, S. Jin, M. Matthaiou, Z. Ding, and C. Xiao, "Beam division multiple access transmission for massive MIMO communications," *IEEE Trans. Commun.*, vol. 63, no. 6, pp. 2170–2184, June 2015.

[28] F. Lai, C.-X. Wang, J. Huang, X. Gao, and F.-C. Zheng, "A novel beam domain channel model for B5G massive MIMO wireless communication systems," *IEEE Trans. Veh. Technol.*, vol. 72, no. 4, pp. 4143–4156, Apr. 2023.

[29] C. Sun, X.-Q. Gao, and Z. Ding, "BDMA in multicell massive MIMO communications: Power allocation algorithms," *IEEE Trans. Signal Process.*, vol. 65, no. 11, pp. 2962–2974, June 2017.

[30] J. Brady, N. Behdad, and A. M. Sayeed, "Beamspace MIMO for millimeter-wave communications: System architecture, modeling, analysis, and measurements," *IEEE Trans. Antennas Propag.*, vol. 61, no. 7, pp. 3814–3827, July 2013.

[31] X. Gao, L. Dai, Y. Zhang, T. Xie, X. Dai, and Z. Wang, "Fast channel tracking for terahertz beamspace massive MIMO systems," *IEEE Trans. Veh. Technol.*, vol. 66, no. 7, pp. 5689-5696, July 2017.

[32] R. Jiao, L. Dai, W. Wang, F. Lyu, N. Cheng, and X. Shen, "Max-min fairness for beamspace MIMO-NOMA: From single-beam to multi-beam," *IEEE Trans. Wireless Commun.*, vol. 21, no. 2, pp. 739-752, Feb. 2022.

[33] X. Wei, C. Hu, and L. Dai, "Deep learning for beamspace channel estimation in millimeter-wave massive MIMO systems," *IEEE Trans. Commun.*, vol. 69, no. 1, pp. 182-193, Jan. 2021.

[34] X. Gao, L. Dai, S. Han, C.-L. I, and X. Wang, "Reliable beamspace channel estimation for millimeter-wave massive MIMO systems with lens antenna array," *IEEE Trans. Wireless Commun.*, vol. 16, no. 9, pp. 6010-6021, Sept. 2017.

[35] A. Sayeed and J. Brady, "Beamspace MIMO channel modeling and measurement: Methodology and results at 28 GHz," in *Proc. IEEE Globecom'16 Wkshps*, Washington, DC, USA, Dec. 2016, pp. 1–6.

[36] J. Bian, C.-X. Wang, R. Feng, Y. Liu, W. Zhou, F. Lai, and X.-Q. Gao, "A novel 3D beam domain channel model for massive MIMO communication systems," *IEEE Trans. Wireless Commun.*, vol. 22, no. 3, pp. 1618–1632, Mar. 2023.

[37] H. Chang, C.-X. Wang, J. Bian, R. Feng, Y. He, Y. Chen, and E. H. M. Aggoune, "A novel 3D beam domain channel model for UAV massive MIMO communications," *IEEE Trans. Wireless Commun.*, early access, 2023, doi: 10.1109/TWC.2023.3233961.

[38] C.-X. Wang, Z. Lv, X.-Q. Gao, X.-H. You, Y. Hao, and H. Haas, "Pervasive channel modeling theory and applications to 6G GBSMs for all frequency bands and all scenarios," *IEEE Trans. Veh. Technol.*, vol. 71, no. 9, pp. 9159-9173, Sept. 2022.

[39] F. Sohrabi and W. Yu, "Hybrid analog and digital beamforming for mmWave OFDM large-scale antenna arrays," *IEEE J. Sel. Areas Commun.*, vol. 35, no. 7, pp. 1432–1443, July 2017.

[40] D. Tse and P. Viswanath, *Fundamentals of Wireless Communication*. New York, NY, USA: Cambridge Univ. Press, 2005.

[41] A. M. Sayeed, "Deconstructing multiantenna fading channels," *IEEE Trans. Signal Process.*, vol. 50, no. 10, pp. 2563–2579, Oct. 2002.

[42] J. Li, B. Ai, R. He, *et al.*, "On 3D cluster-based channel modeling for large-scale array communications," *IEEE Trans. Wireless Commun.*, vol. 18, no. 10, pp. 4902–4914, Oct. 2019.

[43] X. Wei and L. Dai, "Channel estimation for extremely large-scale massive MIMO: Far-field, near-field, or hybrid-field?" *IEEE Commun. Lett.*, vol. 26, no. 1, pp. 177–181, Jan. 2022.

[44] M. Cui and L. Dai, "Channel estimation for extremely large-scale MIMO: Far-field or near-field?" *IEEE Trans. Commun.*, vol. 70, no. 4, pp. 2663–2677, Apr. 2022.

[45] M. Viberg, B. Ottersten, and A. Nehorai, "Performance analysis of direction finding with large arrays and finite data," *IEEE Trans. Signal Process.*, vol. 43, no. 2, pp. 469–477, Feb. 1995.

[46] J. Huang, C.-X. Wang, R. Feng, J. Sun, W. Zhang, and Y. Yang, "Multi-frequency mmWave massive MIMO channel measurements and characterization for 5G wireless communication systems," *IEEE J. Sel. Areas Commun.*, vol. 35, no. 7, pp. 1591–1605, July 2017.

[47] X. Cai, B. Peng, X. Yin, and A. P. Yuste, "Hough-transform-based cluster identification and modeling for V2V channels based on measurements," *IEEE Trans. Veh. Technol.*, vol. 67, no. 5, pp. 3838–3852, May 2018.

[48] Z. Ma, B. Ai, R. He, *et al.*, "Impact of UAV rotation on MIMO channel characterization for air-to-ground communication systems," *IEEE Trans. Veh. Technol.*, vol. 69, no. 11, pp. 12418–12431, Nov. 2020.

[49] J. Zhang, Y. Zhang, Y. Yu, R. Xu, Q. Zheng, and P. Zhang, "3-D MIMO: How much does it meet our expectations observed from channel measurements?" *IEEE J. Sel. Areas Commun.*, vol. 35, no. 8, pp. 1887–1903, Aug. 2017.

[50] D. P. Palomar, J. R. Fonollosa, and M. A. Lagunas, "Capacity results of spatially correlated frequency-selective MIMO channels in UMTS," in *Proc. IEEE VTC'01*, Atlantic City, NJ, USA, Oct. 2001, pp. 553–557.

[51] J. Bian, J. Sun, C.-X. Wang, R. Feng, J. Huang, Y. Yang, and M. Zhang, "A WINNER+ based 3D non-stationary wideband MIMO channel model," *IEEE Trans. Wireless Commun.*, vol. 17, no. 3, pp. 1755–1767, Mar. 2018.

[52] R. He, B. Ai, G. L. Stuber, G. Wang, and Z. Zhong, "Geometrical-based modeling for millimeter-wave MIMO mobile-to-mobile channels," *IEEE Trans. Veh. Technol.*, vol. 67, no. 4, pp. 2848–2863, Apr. 2018.

[53] M. Matthaiou, A. M. Sayeed, and J. A. Nossek, "Sparse multipath MIMO channels: Performance implications based on measurement data," in *Proc. IEEE SPAWC'09*, Perugia, Italy, June 2009, pp. 364–368.

[54] H. Zhang, R. He, B. Ai, S. Cui, and H. Zhang, "Measuring sparsity of wireless channels," *IEEE Trans. Cogn. Commun. Netw.*, vol. 7, no. 1, pp. 133–144, Mar. 2021.